Fall 2019

Smart control architecture for microgrid application

Vikram Roy Chowdhury

Department: Electrical and Computer Engineering

Recommended Citation

Roy Chowdhury, Vikram, "Smart control architecture for microgrid application" (2019). *Doctoral Dissertations*. 2847.
https://scholarsmine.mst.edu/doctoral_dissertations/2847

SMART CONTROL ARCHITECTURE FOR MICROGRID APPLICATION

by

VIKRAM ROY CHOWDHURY

A DISSERTATION

Presented to the Graduate Faculty of the

MISSOURI UNIVERSITY OF SCIENCE AND TECHNOLOGY

In Partial Fulfillment of the Requirements for the Degree

DOCTOR OF PHILOSOPHY

in

ELECTRICAL ENGINEERING

2019

Approved by

Jonathan W. Kimball, Adviser
Jagannathan Sarangapani
Mariesa L. Crow
Rui Bo
Jonghyun Park

PUBLICATION DISSERTATION OPTION

This dissertation has been prepared using the publication option and is composed of three papers.

Paper I : Pages 4 - 32, Control of a three phase grid connected inverter under non-ideal grid conditions with online parameter update. Published in *IEEE Trans. Energy Conversion*,

Paper II : Pages 33-56, Grid Voltage Sensorless Synchronization of a Three-phase Grid Connected Inverter under unbalanced Grid Voltage Condition. have been submitted to *IEEE Transactions on Sustainable Energy*,

Paper III : Pages 57-78, Optimal Battery Scheduling in a Microgrid based on Markov Decision Process for cost Minimization. are intended for submission to *IEEE Transactions on Sustainable Energy*,

ABSTRACT

This research proposes non-linear control architectures dedicated towards improving transient response, reliability and computational burden for grid connected inverters applicable for ac micro-grids. Also this work proposes an optimization procedure applied to a small microgrid to reduce the billing cost for power incorporating battery degradation mechanism.

Three works are discussed in this research that discusses methodologies to improve the operation of a three phase grid connected inverters. The first work discusses a globally stable estimation architecture for estimating the plant parameters for a grid connected inverter during its operation. Then a Lyapunov based control architecture is utilized and online parameter update scheme is used to optimize the controller performance. The second work discusses a Lyapunov based control architecture during a contingency that the grid voltage sensor fails. In this work an internal model based grid voltage estimation architecture has been proposed which successfully estimates the grid voltage and controls the grid current. The last work shows a methodology to optimally utilize a battery in a microgrid based on Markov Decision Process. Dynamic algorithm is used to solve the problem so that the cost is minimized at the end of the day.

Furthermore, in this research detailed stability analysis of the first two works along with the controller design has been presented. Also in this work, battery degradation is modelled empirically and the overall cost function is obtained for the optimization of billing cost for a small microgrid.

Detailed plant modeling, controller design, simulation and experimental results are presented for all of the proposed schemes.

ACKNOWLEDGMENTS

I would like to thank Dr. Jonathan Kimball for giving me the opportunity to work in his research group. I would like to acknowledge the financial and technical support they have given to me during my doctoral studies. I would also like to thank , Dr. Jagannathan Sarangapani, Dr. Mariesa L. Crow, Dr. Rui Bo and Dr. Jonghyun Park for being my committee members and for their valuable inputs. I would like to thank my lab-mates and friends in Missouri University of Science and Technology, Rolla, for providing help and support during the course of my doctoral studies at S&T.

Finally, I would like to thank my parents for making me what I am today. A little time of my PhD that I had with my father was the best. I would like to thank my mother and my sister for always being there helping and supporting me emotionally when I was disappointed during my whole PhD time. My special thanks goes to my sister in Rolla, Sara Yazdani, for her technical criticism of my work and constructive inputs and encouragements to improve my work further.

TABLE OF CONTENTS

Page

SECTION

PAPER

SECTION

LIST OF ILLUSTRATIONS

Figure Page

PAPER I

PAPER II

PAPER III

LIST OF TABLES

Table Page

PAPER I

PAPER II

PAPER III

SECTION

1. INTRODUCTION

With focus in reducing emission by fossil fuel, renewable energy has gained immense importance in recent years. Grid connected inverters constitute one of the most important part of any modern day ac microgrids. However, with more renewable power resources' penetration, it becomes immensely challenging to use these sources optimally. As a first resort advanced control architecture needs to be accomplished. It is also well known that the most common form of renewable power source is that of solar energy [1]. Therefore, even with high initial cost for setting up solar energy remains the most common form of renewable power generation scheme. Various current control architecture has been reported in the literature to operate voltage source converters interfacing renewable energy sources to the grid [2]. However, in general all the current control architecture relies on the small signal modeling of the plant i.e the L or LCL filters that interfaces these converters to the grid.

The problem of synchronizing these converters in a non-ideal grid also is a popular area of research. In most of the practical cases, the grid voltage is non-sinusoidal in nature and challenge arises in to keep the converter operating stably even under such a condition. Grid synchronization techniques' overview reported in various literature has been presented in [3]. Also a methodology to synchronize an inverter to a polluted grid has been reported in [4] where both the voltage unbalance/distortion and frequency variations has been reported. Frequency control for grid connected systems also has become immensely challenging by the penetration of more and more renewable energy resources. The work reported in [5] talks about the inertial response due to $HVDC$ wind farms and their primary frequency control. It is also sometimes customary to connect parallel power converters in a low voltage microgrid. A low voltage microgrid unlike a high voltage one is more resistive in nature. Therefore, the power flow equations for a low voltage microgrid is reversed i.e. to say active power becomes proportional to the difference in voltage between the inverter and the grid and reactive becomes proportional to the difference in angle between the inverter and the grid. In such a grid, the parallel operation of converter has been reported and various case studies are discussed as presented in [6]. With many parallel converters connected, it becomes a challenge to either control all of them centrally which requires high cost communication networks between these converters. The other way is to control these converters in a decentralized fashion. A work related to the latter methodology based on resistive output impedance shaping has been presented in [7]. Implementation of advanced control architecture for a UPS has been presented in [8]. The reported work uses a multi-loop control control architecture. However, due to such an architecture, the outer loops inherently remains slow and the overall dynamic response is affected. Another methodology reported a smooth transition mechanism during microgrid application [9]. Finally, a high frequency link inverter control based on proportional multiresonant architecture has been reported for a three phase four-wire high frequency link inverter in [10]. The overall transient and steady state performance in this work has been shown to be very good. However, such a control architecture requires lots of computation and high memory to implement. Also since the exact order of harmonics are not known in the grid, therefore, the amount of resonant controllers that can be implemented are always a limitation.

To address all the challenges reported above, the work in this dissertation is carried out and explored for non-linear control architecture and parameter estimation with its effect on improving the dynamic response of a grid connected converter. In the first work the plant model is developed to achieve the global stability of the overall system. An overall parameter update scheme is proposed in the work to optimize the overall performance of the system. In the next work, a control algorithm is proposed based on Lyapunov stability criteria for a grid connected converter during the contingency when the grid voltage sensor fails. During a situation like that the phase locked loop information is lost. A grid voltage estimation technique based on the filter component value is proposed based on internal model based structure. Detailed stability analyses both large signal and small signal for the proposed estimation architecture has been presented. The last work presents an optimal usage of a battery based on Markov Decision Process to optimally use a battery incorporating the battery degradation based on curve fitting techniques. Dynamic programming is utilized to solve the problem and achieve minimum cost for power production in a day. A detailed sensitivity analyses based on the rate structure followed and the battery cost is presented so as to understand the effectiveness of the proposed optimization technique.

PAPER

I. CONTROL OF A THREE-PHASE GRID-CONNECTED INVERTER UNDER NON-IDEAL GRID CONDITIONS WITH ONLINE PARAMETER UPDATE

ABSTRACT

Three-phase grid-connected inverter modeling depends on the equivalent resistance and inductance between the inverter and the grid. However, these parameters are not fixed during the operation of the inverter and vary with the operating conditions. In this paper, a new globally stable adaptive controller is proposed to estimate these values online and update the controller during its operation. A model reference adaptive system (MRAS) based on two fictitious quantities with no physical significance is utilized, namely $M = v \cdot i^*$ and $N = v^* \times i$, where v and i are the steady-state values of voltage and current in synchronously rotating frame of reference. Detailed stability analysis of the proposed estimation technique has been presented using a Lyapunov energy function-based approach proving the global stability of the technique. Small-signal modeling and analysis of the proposed scheme has also been presented so as to understand the local dynamics of the system. The guidelines to select the parameter of the proposed MRAS system along with updating the controller are elaborated in this paper. Detailed simulation based on MATLAB/Simulink and PLECS, along with experimental studies through a Texas Instruments TMS320F28377S microcontroller, validates the feasibility of the proposed control architecture.

1. INTRODUCTION

Control of grid-connected converters has been one of the most important fields of research in the past few years. The most popular technique being that of current-controlled architecture [1–3]. The design of the current controller depends on an accurate plant model and thus needs to have the knowledge of the equivalent resistance and inductance from the inverter to the grid [4–10]. However, with the operation of the inverter, these parameters vary from their nominal values assumed to design the controller. To address this problem and achieve optimum performance, it is a necessity to estimate the plant parameters online and update the controller.

Addressing the issue, the authors of [11–13] have proposed an estimation technique for the equivalent resistance and inductance from inverter to the grid. In [11] and [12] neural network methodologies are utilized to estimate the parameters. However, the neural network-based estimator makes the implementation of the algorithm computationally heavy and the proposed technique is not physically verified on hardware. It also becomes an immense computational challenge to online estimate the parameters and also update the controller using neural network-based approach. The concept of MRAS has been presented in [14] and [15] for parameter estimation. It is a very powerful tool in control systems that is popularly used for parameter estimation. For power electronics applications the MRAS technique is widely used for speed estimation of sensorless drive systems. The MRAS methodology applied to motor drive systems is presented for cage rotor induction machines in [14–19], for doubly fed induction machines in [20–23] and for permanent magnet machines in [24], [25]. Few studies report on the application of the MRAS methodology to grid connected inverters [12], [13]. The presented methodologies in these papers rely on a computationally expensive, iterative MRAS structure. Such a structure substantially increases the computational burden on the microcontroller and puts a limitation on the switching frequency of the system which can adversely affect the size of the interfacing filter components. These papers indicate that a high number of iterations are required for convergence. An iterative process needs both an initial guess and upper and lower bounds. However, if the initial guess is not chosen correctly, then the overall MRAS architecture might not converge to the correct values of the plant parameters and the overall system might become unstable. The previously reported controller architecture relies on an internal model based proportional integral controller which is based on the plant model linearized around a chosen operating point. Therefore with large variations of plant parameters system might become unstable even with parameter updates. Also, no discussion of the estimation technique under unbalanced/distorted grid voltage conditions is mentioned. The proposed MRAS technique described in this paper has been proven to be globally asymptotically stable by Lyapunov energy function criteria. Also the proposed structure being closed loop in nature therefore it is not required to have any iterative procedure for its convergence making the computational burden on the microcontroller lower. References [14–22] present MRAS techniques applied mainly to electric drive system to adaptively estimate the machine speed.

In this paper, two fictitious quantities M and N are chosen for estimation of the equivalent resistance and inductance between the inverter and the grid. The choice of these quantities is totally dependent on experience, and discussion of how to choose these models most optimally is beyond the scope of this paper. The proposed estimation method is simpler and relies on a closed-loop structure compared to those presented in [10–13], which rely on an open-loop iterative structure involving huge computation. The proposed estimation technique gives accurate estimation of the plant parameters even under unbalanced/distorted grid voltage conditions.The rest of the paper is organized as follows: Section 2 presents the formulation of the proposed estimation technique, Section 3 presents the analysis and derivation of stability for the proposed estimation technique, Section 4 presents the Lyapunov energy function-based control strategy, Section 5 presents the simulation results, Section 6 presents the experimental verification followed by conclusion in Section 7.

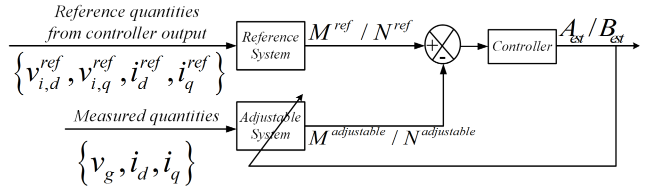

Figure 1. Simplified block diagram architecture of MRAS

2. FORMULATION OF THE PROPOSED ESTIMATION TECHNIQUE

2.1. MODEL REFERENCE ADAPTIVE SYSTEM (MRAS) USED AS AN ESTIMATOR

The proposed estimation technique presented in this paper is based on a model reference adaptive system (MRAS). MRAS architecture consists of a reference system, an adjustable system, and a controller [15]. All the inputs to the reference system are known variables. For a multi-input multi-output (MIMO) system the reference system takes j measurable inputs to give Z_1 as the output. However, the inputs taken by the adjustable system are k known variables and only one unknown variable that is intended to be measured and gives Z_2 as the output. If the estimation of the unknown variable converges to the actual value in steady-state, then $Z_1 = Z_2$ else $Z_1 \neq Z_2$. The concept of MRAS is to process the error between Z_1 and Z_2 to reduce it to zero, thereby ensuring the convergence of the unknown variable to its actual value. A simplified block diagram of the aforementioned MRAS architecture is presented in Figure 1.

In this paper a novel globally stable estimation technique has been proposed to obtain the equivalent resistance and inductance of a three-phase grid-connected inverter.

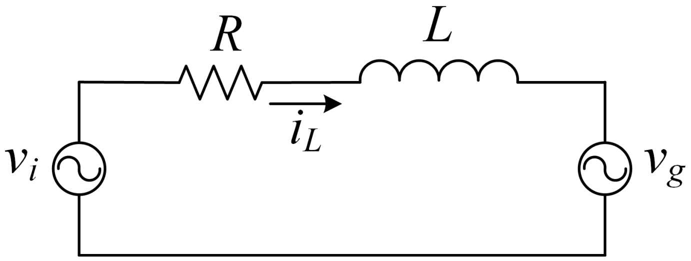

Figure 2. Equivalent circuit of one phase of a three-phase inverter

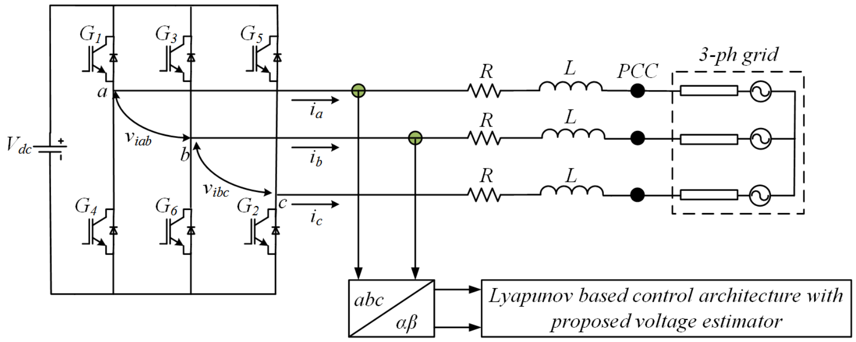

Figure 3. Three-phase grid connected inverter

2.2. UTILIZATION OF MRAS FOR ESTIMATION OF EQUIVALENT IMPEDANCE

A three-phase grid-connected inverter is presented in Figure 3. A per-phase equivalent circuit of the grid-connected inverter in Figure 3 is presented in Figure 2. The per-phase inductance in the diagram is marked as L and the equivalent series resistance per phase as r. The fundamental component of the inverter voltage is v_i and that of the grid voltage is v_g.

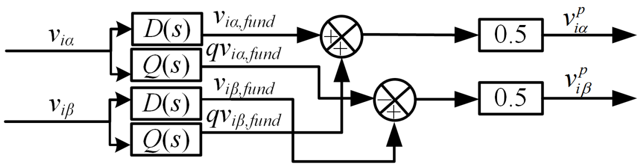

Figure 4. Simplified block diagram representation of DSOGI architecture

The two fictitious quantities M and N utilized in this paper for the estimation of equivalent resistance and inductance of the system are elaborated and quantified here. Global stability for the two estimated quantities are proven in this paper. The latter shows the system's ability to estimate the values under any operating condition. Next, the overall system modeling for the proposed estimation technique is presented. The transformation from the abc to dq frame is accomplished utilizing

$$\begin{bmatrix} d \\ q \end{bmatrix} = \frac{2}{3} \begin{bmatrix} \sin(\omega t) & \cos(\omega t) \\ \sin(\omega t - \frac{2\pi}{3}) & \cos(\omega t - \frac{2\pi}{3}) \\ \sin(\omega t + \frac{2\pi}{3}) & \cos(\omega t + \frac{2\pi}{3}) \end{bmatrix}^T \begin{bmatrix} a \\ b \\ c \end{bmatrix} \tag{1}$$

The transformation presented in (1) is applied to the voltage and current of the inverter and the system modeling is accomplished in synchronous dq frame of reference is given as

$$v_{dinv} = L\frac{di_d}{dt} + i_d R - \omega L i_q + v_{gd} \tag{2}$$

$$v_{qinv} = L\frac{di_q}{dt} + i_q R + \omega L i_d + v_{gq} \tag{3}$$

In (2) and (3), during balanced grid voltage conditions at steady-state, the d and q quantities are all pure dc quantities. However, under unbalanced grid voltage conditions, the quantities become oscillatory with double frequency components. In that case, a dual second-order generalized integrator (DSOGI) [26–28] architecture is utilized to extract the positive sequence components as well as to estimate the equivalent resistance and inductance. The simplified structure of a DSOGI architecture is presented in Figure 4. In general, the second-order generalized integrator (SOGI) structure is a collection of two filters: a bandpass and a low pass. The transfer function for the SOGI architecture is given by

$$G_{ph} = \frac{k\omega_{ref} s}{s^2 + k\omega_{ref} s + \omega_{ref}^2} \tag{4}$$

$$G_{quad} = \frac{k\omega_{ref}^2}{s^2 + k\omega_{ref} s + \omega_{ref}^2} \tag{5}$$

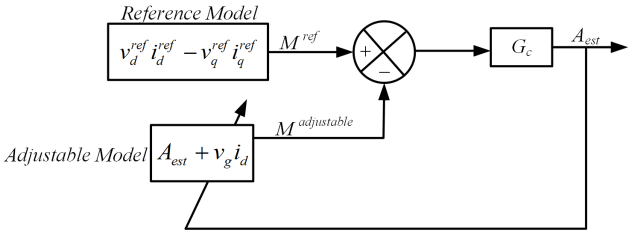

Figure 5. Simplified block diagram to determine A_{est}

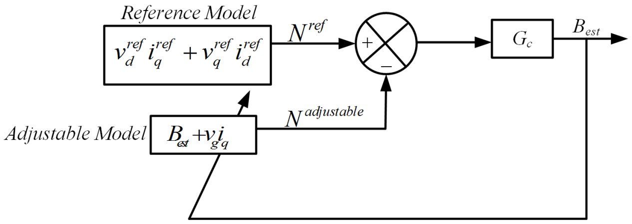

Figure 6. Simplified block diagram to determine B_{est}

The quantities in (4) and (5) create the in-phase and quadrature component respectively at the fundamental frequency of ω_{ref}. Depending on the choice of k, harmonics can also be highly suppressed. Thus any unbalanced set of three sinusoidal quantities (with distortion) can be converted to a stationary two-phase $\alpha\beta$ quantity.Then utilizing (4) and (5), the in-phase and quadrature components can be extracted for both α and β quantities:

$$\alpha^{pos} = \frac{1}{2}(\alpha^{ph} + \beta^{quad}) \tag{6}$$

$$\beta^{pos} = \frac{1}{2}(-\alpha^{quad} + \beta^{ph}) \tag{7}$$

Equations (6) and (7) are utilized to extract the positive sequence components of v_i and v_g . The positive sequence grid voltage quantities are utilized to generate the unit vectors from the phase locked loop (PLL) structure so as to extract the dq components that are pure dc quantities. The DSOGI architecture utilizes two of these filters each for the α and β axes separately. The limitation of the proposed estimation technique lies in the fact that the

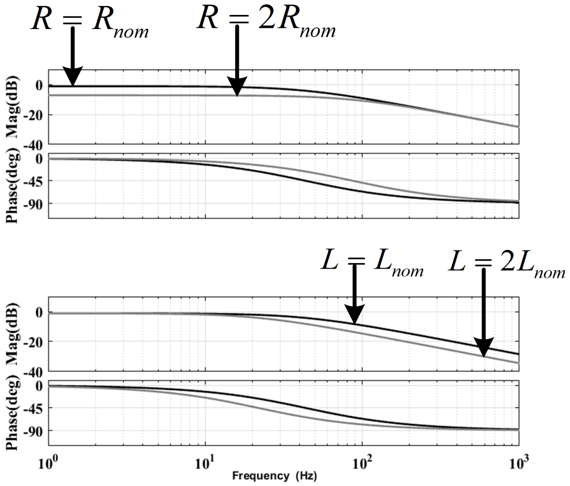

Figure 7. Frequency response of the open loop plant

current controller is much faster than the estimator. The Bode plot of Figure 7 presents the open-loop plant frequency response characteristic for variations in L and R. Generally, the possible variation in R can be taken to be twice its nominal value and that of L can be taken as ±15% from nominal. It is observed from Figure 7 that with the variations of R and L, the open-loop plant remains stable. Therefore to design the current controller, its bandwidth is generally kept a decade lower than the switching frequency. The bandwidth of the estimator is kept in the order of one by hundredth of the current controller bandwidth. So for all practical purposes, to model the estimator dynamics, the current controller dynamics can be neglected. The estimation of A_{est} and B_{est} are presented in a simplified block diagram format respectively in Figures 5 and 6. The derivation of the estimated quantities from the reference and the measured variables are presented:

$$M = v_i \cdot i^* \tag{8}$$

where '*' indicates the conjugate of the vector, with $v_i = v_{i,d} + jv_{i,q}$ (the inverter-side voltage) and $i^* = i_d - ji_q$. Simplification of (8) utilizing the reference quantities yields

$$M^{ref} = v_{i,d}^{ref} i_d^{ref} - v_{i,q}^{ref} i_q^{ref} \tag{9}$$

All the quantities in (9) are known and are obtained from the controller architecture. The same quantity is then recomputed using measured,

$$M^{adjustable} = v_{i,d}^{ref} i_d - v_{i,q}^{ref} i_q. \tag{10}$$

Using (2) and (3) and neglecting the dynamics considering the current controller to be faster than the estimator, the expression for $M^{adjustable}$ may be expressed in terms of the circuit parameters,

$$\begin{aligned} M^{adjustable} &= (i_d R - \omega L i_q + v_{gd}) i_d \\ &-(i_q R + \omega L i_d^{ref} + v_{gq}) i_q \end{aligned} \tag{11}$$

Simplifying (11) with the assumption that the d axis is latched with the grid voltage by the PLL, we have

$$M^{adjustable} = (i_d^2 - i_q^2) R_{est} - 2 X_{est} i_d i_q + v_g i_d \tag{12}$$

Note that in (12), $v_{gd} = v_g$ and $v_{gq} = 0$. The simplified expression for (12) is given by

$$M^{adjustable} = A_{est} + v_g i_d \tag{13}$$

where

$$A_{est} = (i_d^2 - i_q^2) R_{est} - 2 X_{est} i_d i_q \tag{14}$$

All the quantities in (13) are known except A_{est}. The error between (9) and (13) is passed through a compensator, and A_{est} is determined. Similar expressions can be obtained for N and are given by

$$N = \left| v_i^* \times i \right| \tag{15}$$

As the cross product of two vectors is a vector quantity, N is computed as the magnitude of the result of the cross product. Using reference quantities, (15) can be simplified to

$$N^{ref} = v_{id}^{ref} i_q^{ref} + v_{i,q}^{ref} i_d^{ref} \tag{16}$$

Similar to (9), all the quantities in (16) are known and can be obtained from the controller architecture. Expression for the same quantity can be obtained from the measurable quantities and can be expressed as

$$N^{adjustable} = B_{est} + v_g i_q \tag{17}$$

where

$$B_{est} = 2R_{est} i_d i_q + (i_d^2 - i_q^2) X_{est} \tag{18}$$

All quantities except B_{est} in (17) are known. The error between (16) and (17) is processed through a compensator and B_{est} is determined. The simplified expressions for the quantities A_{est} and B_{est} in terms of the equivalent resistance and reactance are presented in (14) and (18) Simplifying (14) and (18) algebraically the corresponding expressions for the equivalent resistance and reactance respectively become;

$$R_{est} = \frac{A_{est}(i_d^2 - i_q^2) + 2B_{est} i_d i_q}{(i_d^2 + i_q^2)^2} \tag{19}$$

$$X_{est} = \frac{B_{est}(i_d^2 - i_q^2) - 2A_{est} i_d i_q}{(i_d^2 + i_q^2)^2} \tag{20}$$

Any estimation technique must be stable so that the variables converge to their actual value in steady state. The next section presents the stability of the proposed estimation technique discussed in this paper.

3. ANALYSIS AND DERIVATION OF STABILITY OF THE PROPOSED ESTIMATION TECHNIQUE

3.1. GLOBAL STABILITY

This subsection presents the methodology for determining the global stability of the proposed estimation technique. As the estimator structure is that of MRAS, the global stability rules for such a structure are already reported in [14, 15]. The rules presented in the literature use Popov stability criteria to comment on the system's global stability. In this paper, the global stability of the proposed estimation technique has been verified using Lyapunov energy function-based analysis. From the simplified block diagram of Figure 8, we have

$$A_{est} = A_{err}\frac{K_i^{est}}{s} \tag{21}$$

Substituting $A_{err} = A - A_{est}$ in (21) yields

$$A - A_{err} = A_{err}\frac{K_i^{est}}{s} \tag{22}$$

In time domain, (22) can be represented as

$$\dot{A}_{err} = -A_{err}K_i^{est} \tag{23}$$

To check the global stability of the estimator it is required to define a Lyapunov energy function. In general any Lyapunov function must satisfy the following criteria to achieve global stability:

$$\begin{aligned} &V(0) = 0 \\ &V(x) > 0 \ \forall x \neq 0 \\ &V(x) \rightarrow \infty \ for \ \|x\| \rightarrow \infty \\ &\dot{V}(x) < 0 \ \forall x \neq 0 \end{aligned} \tag{24}$$

Let us now consider a Lyapunov energy function, $V(A_{err})$ which is defined as

$$V(A_{err}) = \frac{1}{2}A_{err}^2 \tag{25}$$

Equation (25) follows the first three conditions of (24). To check the last criteria of (24), (25) is differentiated with respect to time and the expression is given by

$$\dot{V}(A_{err}) = A_{err}\dot{A}_{err} \tag{26}$$

Substituting $\dot{A}_{err}$ from (23) in (26) we have

$$\dot{V}(A_{err}) = -A_{err}^2K_i^{est} \tag{27}$$

For all real non-zero values, (27) is always negative, satisfying the last condition of (24). Therefore the proposed estimation technique is globally asymptotically stable. Similar analysis can be accomplished for B and can be shown to be globally asymptotically stable as A.

3.2. SMALL-SIGNAL ANALYSIS FOR THE PROPOSED ESTIMATION TECHNIQUE

To ensure the desired transient and steady-state performance, the compensator utilized in the estimator must have proper gains. Therefore the small-signal system modeling is presented in this section along with the compensator design. Considering similar expressions as (13) for the reference value, we have

$$M^{ref} = A + v_g i_d^{ref} \tag{28}$$

where $A = (i_d^{ref2} - i_q^{ref2})R - 2X i_d^{ref} i_q^{ref}$. Let us consider $i_d = I_{do} + \Delta i_d$ and $i_q = I_{qo} + \Delta i_q$ where I_{do} and I_{qo} are the steady state average values of the d and q axes currents. Using (13) and (28) with the incorporated small signal perturbation in current we can define

$$M_{err} = M^{ref} - M^{adjustable} = A_{err} + v_g \Delta i_d \tag{29}$$

where $A_{err} = A - A_{est}$. With the prior assumption of current control loop being much faster than the estimator, in (29) we can put $\Delta i_d = 0$. The simplified small signal model for the plant then turns out to be

$$G^A_{plant} = \frac{M_{err}}{A_{err}} = 1 \tag{30}$$

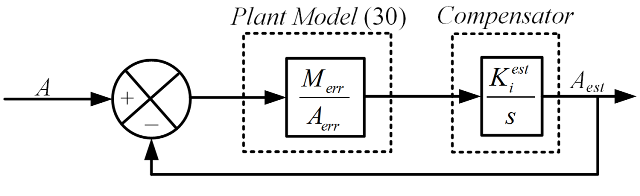

Figure 8. Closed loop representation for the estimation of A

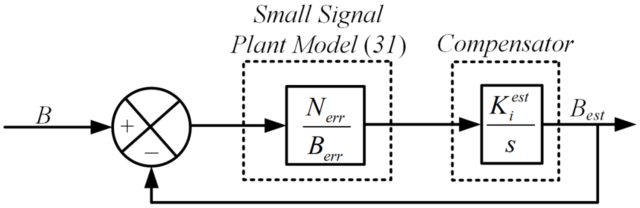

Figure 9. Closed loop representation for the estimation of *B*

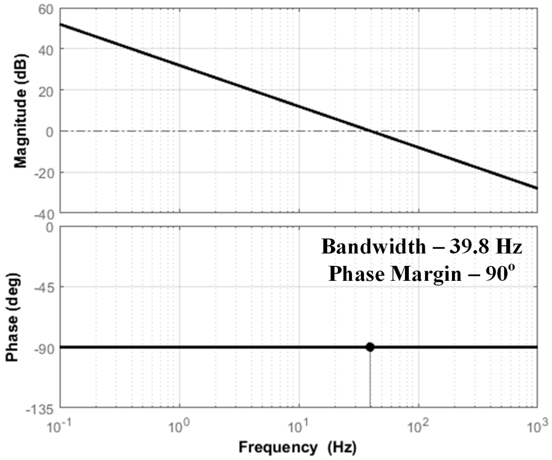

Figure 10. Bode plot for the plant and the controller used for estimating the impedance

Equation (30) indicates that the plant is a constant and is equal to unity under the mentioned assumptions, particularly that the current loop is much faster than the estimator. Similar analysis can be carried out for the estimation of *B* and the plant model can be computed as

$$G_{plant}^{B} = \frac{N_{err}}{B_{err}} = 1 \tag{31}$$

A simplified block diagram of the small signal model of the estimated quantities is presented in Figures 8 and 9 for *A* and *B* respectively. The plant model for the estimation of both the variables shows that the plant model is identical and is independent of operating point. To design the compensator i.e., select the compensator gain, the Bode plot of the estimator is plotted and shown in Figure 10. The bandwidth of the estimator is in the order of nearly

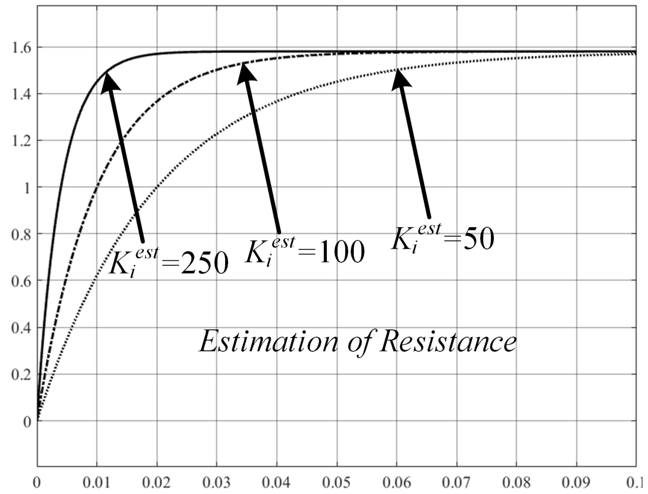

Figure 11. Effect of variation of K_i^{est} on the estimation of resistance

three decades lower than the switching frequency. The plant parameters, compensator gain and the switching frequency are presented in Table 1. These parameters are utilized to estimate the impedance by the proposed methodology presented in this paper. The small signal modeling presented in this section elaborates on the local dynamic behavior of the system and gives the methodology to select the compensator gain.

To better illustrate the effect of the compensator gain on the dynamic performance of the estimated resistance and reactance, three values of K_i^{est} equal to 50, 100 and 250 were chosen and the effect on the estimated resistance and reactance are presented respectively in Figures 11 and 12. For all cases, $i_d = 10$ and $i_q = 0$. As the value of K_i^{est} is increased, the estimation convergence speed is increased. Therefore theoretically the value of K_i^{est} can be chosen arbitrarily high. However, a higher gain increases sensitivity to noise. Also the estimator bandwidth should not interfere with the Lyapunov energy function based controller bandwidth. Therefore, the overall gain of the estimator is chosen to set its bandwidth nearly three decades lower than the current controller bandwidth. The next section presents a parameter-dependent control strategy for a three phase grid connected inverter where the parameters are updated utilizing the proposed estimation algorithm.

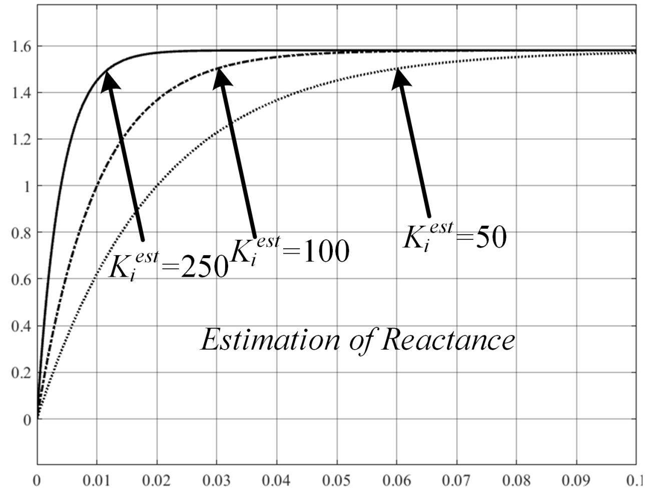

Figure 12. Effect of variation of K_i^{est} on the estimation of reactance

4. SIMULATION RESULTS

The proposed estimation algorithm is verified via simulation studies based on MATLAB/Simulink and Plecs domain. Application of the proposed estimation technique has been presented by utilizing a parameter-dependent control algorithm applied on a three-phase grid-connected inverter. Implemented algorithm is a Lyapunov energy function-based control scheme that is highly parameter sensitive. The two major control equations governing the operation has been presented. The details of how to derive the equations are beyond the scope of the paper and can be found in [29] and [30]. However, in [30] the grid voltage sensor was not present and a methodology for voltage sensorless control has been presented. In this paper, similar methodology has been presented but with the grid voltage sensor. The modulation index in α and β frame for the inverter with Lyapunov energy function-based control architecture is given by

$$m_\alpha = \frac{1}{V_{dc}}\left(L_{est}\frac{di_\alpha^*}{dt} + i_\alpha^* R_{est} + v_{g\alpha}\right) - \frac{R_c}{V_{dc}}x_\alpha \tag{32}$$

$$m_\beta = \frac{1}{V_{dc}}\left(L_{est}\frac{di_\beta^*}{dt} + i_\beta^* R_{est} + v_{g\beta}\right) - \frac{R_c}{V_{dc}}x_\beta \tag{33}$$

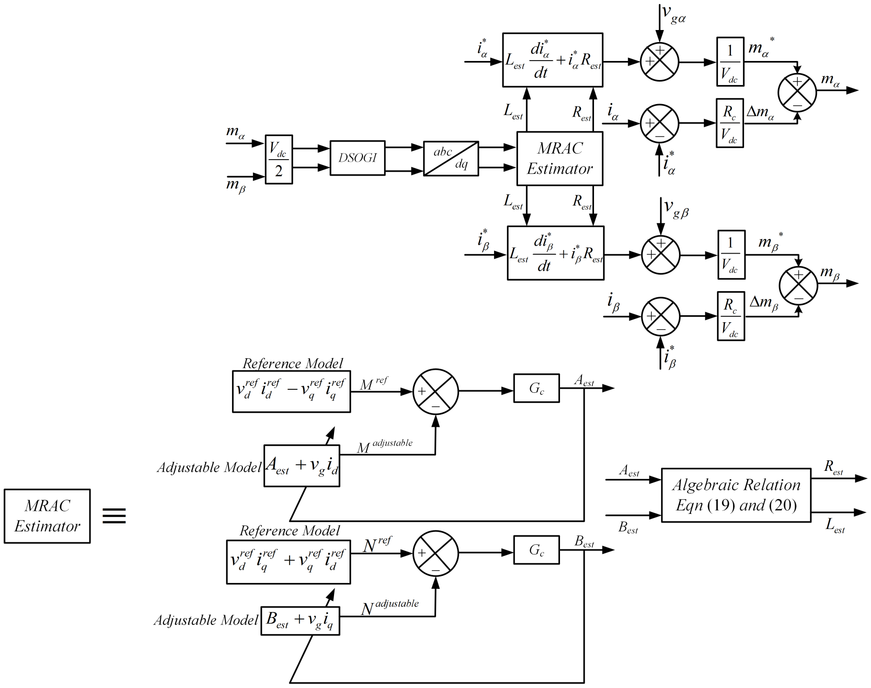

Figure 13. Simplified block diagram of the Lyapunov energy function based current controller embedded with the MRAS estimator

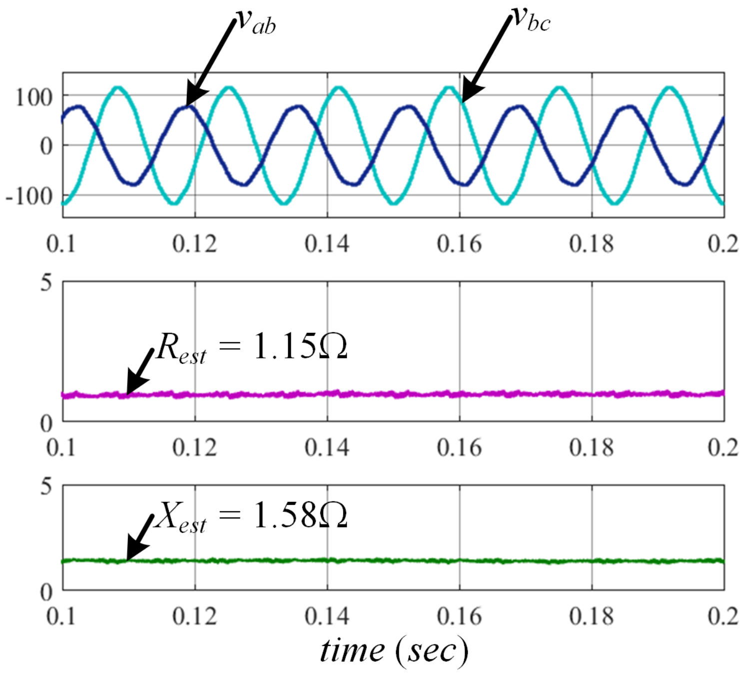

Figure 14. Estimated resistance and reactance under unbalanced/distorted grid voltage condition

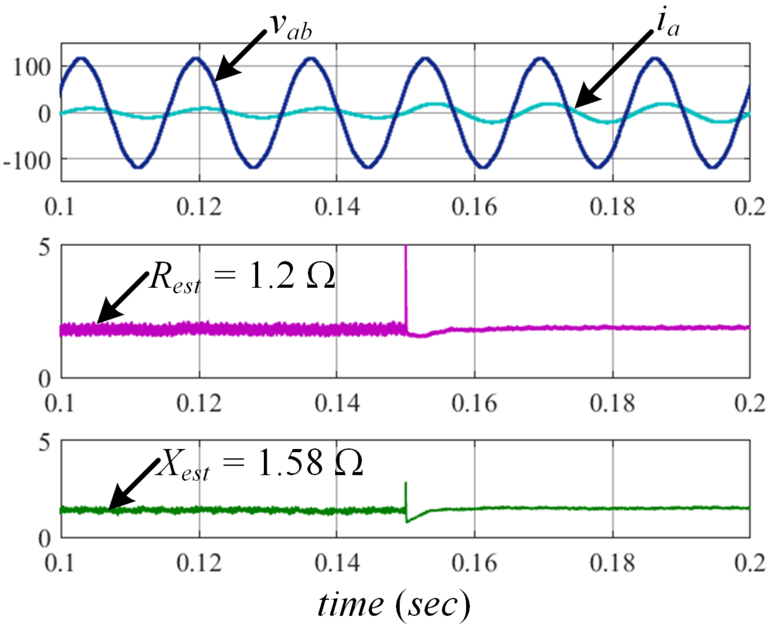

Figure 15. Performance of the controller during a line current transition

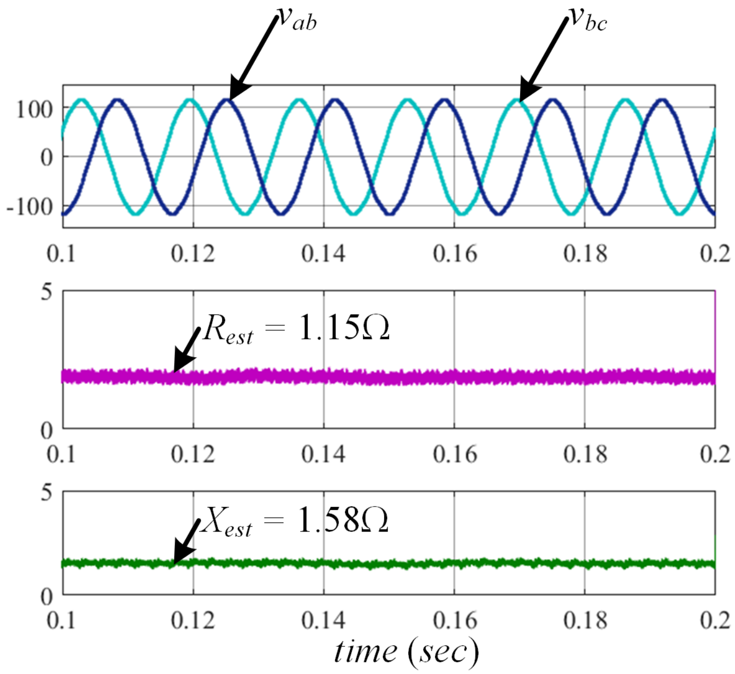

Figure 16. Estimated resistance and reactance under balanced grid voltage condition

Table 1. Plant Parameters

Parameter	**Value**
L	4.2 mH
r	1.15 Ω
K_i^{est}	500
f_s	20 kHz

where $x_\alpha = i_\alpha - i_\alpha^*$ and $x_\beta = i_\beta - i_\beta^*$. The values for L_{est} and r_{est} are updated from the output of the estimator. Using these control laws, the results for the operation of a three-phase grid-connected inverter are presented for various case studies.The value of R_c chosen for the modulation index as shown in (32) and (33) is 100. From the Lyapunov-based control strategy presented in [29] and [30], it can be shown that the value of R_c chosen ensures global asymptotic stability of the system. To understand the operation of the proposed overall control architecture, a simplified block diagram of the Lyapunov energy function based current controller embedded with the MRAC estimator is presented in Figure 13. The result for the estimation of the equivalent resistance and reactance under ideal grid voltage condition is presented. It is observed from Figure 16 that under balanced grid voltage conditions, the proposed estimation technique estimates the equivalent resistance and reactance accurately. Figure 14 shows that the proposed estimation technique works accurately even under unbalanced/distorted grid voltage condition. Figure 15 presents the performance of the estimator during a current transient. Even during transient conditions, the proposed estimation technique accurately give the values of the equivalent resistance and inductance. The dynamic performance of the estimator has also been verified. However, as inductance switching is difficult, a resistance equal to the nominal value of the RL filter resistance connecting the inverter to the grid is switched during the operation of the system and the corresponding result is presented.The estimator tracks and converges to the new resistance value showing the dynamic performance. As the control strategy implemented

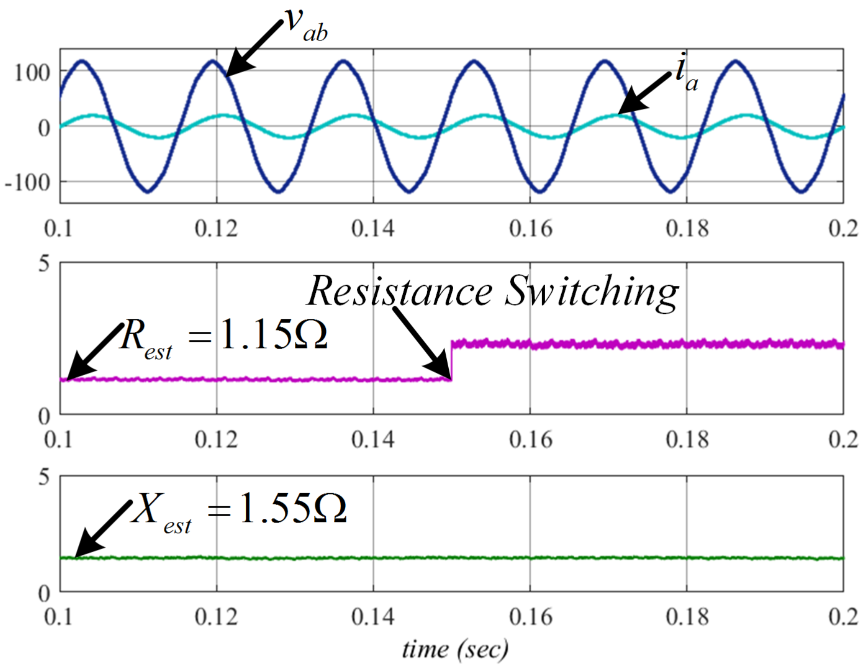

Figure 17. Line voltage and line current during addition of a resistance equal to the nominal value of the RL filter resistance

in this paper is parameter-dependent, it is necessary to show its performance with and without the estimation enabled. Figure 17 shows the dynamic performance of the proposed estimation technique. Figure 18 presents that without the estimation enabled, the Lyapunov-based control strategy is unable to track the reference current when the resistance value is different than the actual. But whenever the estimation is enabled and the Lyapunov function is updated, the reference correctly tracks the actual current. This result shows the utility and use of the estimated impedances for achieving optimum control performance. Also to understand whether actually the reference current and actual current track each other when there is a transient in the current, a case study is considered. First a current command is given with the estimation disabled then a transient change in current is applied. At the same time when the transient in current is applied, the estimation is also enabled. The corresponding performance result is presented in Figure 19. This result is accomplished in a virtual dq frame of reference and is observed that when the estimation is disabled the

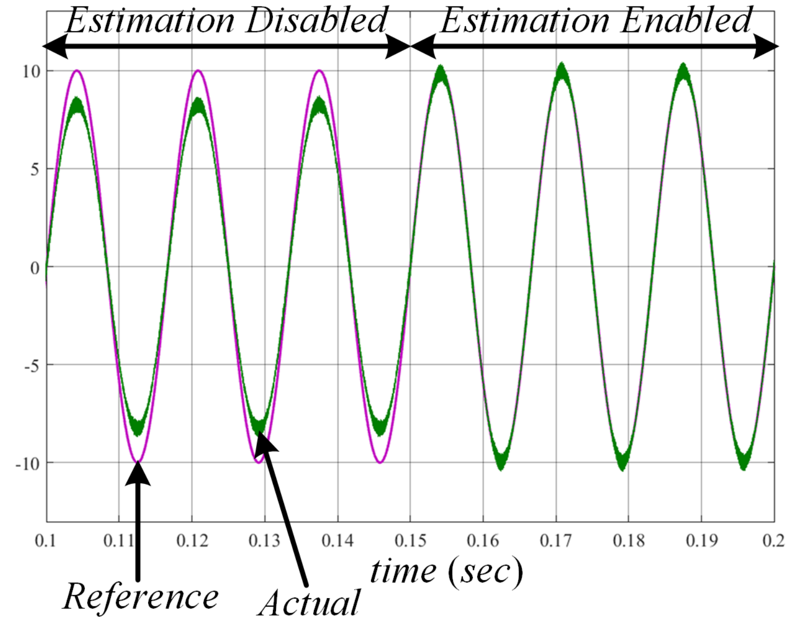

Figure 18. Line current reference and actual with and without the estimation

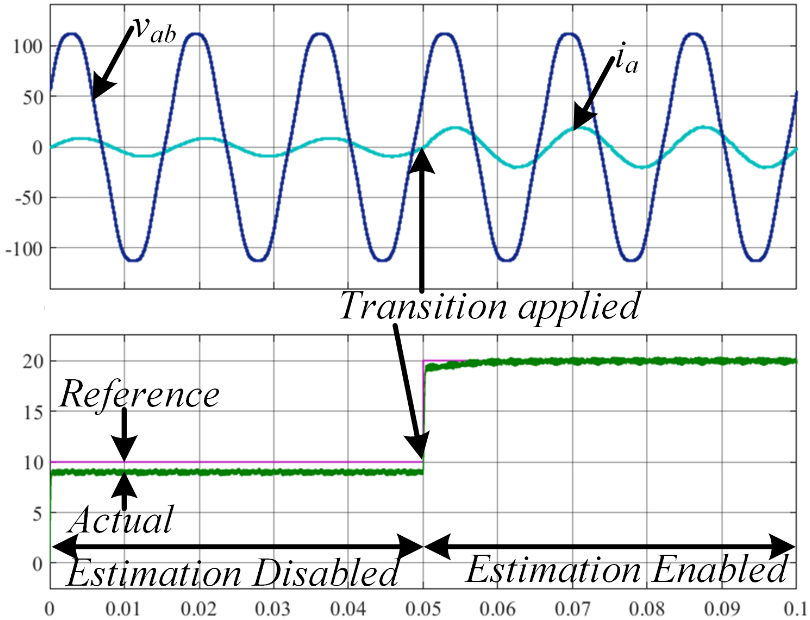

Figure 19. Transient in current and estimation enabling at the same time in a virtual *dq* frame from simulation

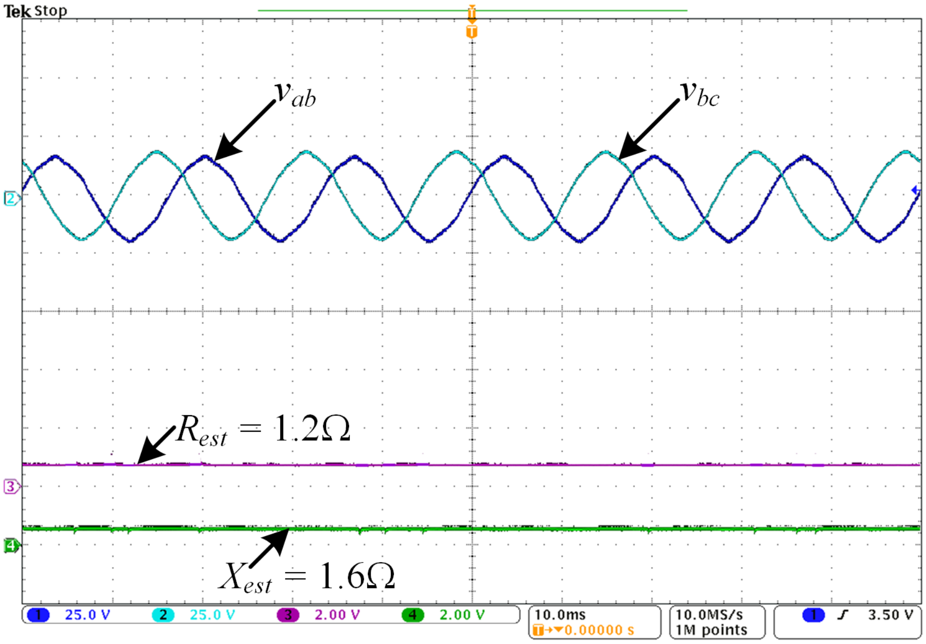

Figure 20. Estimated resistance and reactance under balanced grid voltage condition from experimental studies (R_{est} : 0.6 Ω/div, X_{est} : 1.5 Ω/div)

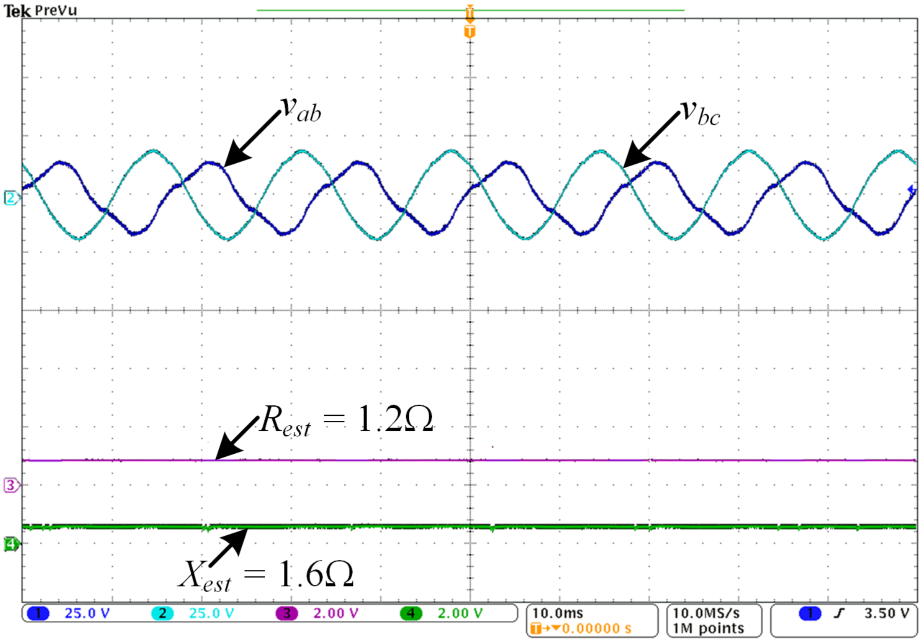

Figure 21. Estimated resistance and reactance under unbalanced/distorted grid voltage condition from experimental studies (R_{est} : 0.6 Ω/div, X_{est} : 1.5 Ω/div)

current reference is not tracked. However, as soon as the reference current is changed and the estimation is enabled, the reference starts tracking the actual current. The next section presents experimental studies for the system showing various case study results similar to simulation studies.

5. EXPERIMENTAL RESULTS

The proposed system discussed in this paper is verified experimentally on a reduced scale laboratory prototype. The experimental setup was built around a TMS320F28377s microcontroller from Texas Instruments. BSM30GP60 inverter module from Infineon is utilized to form the three-phase inverter bridge. Hall-effect current sensors (LA-55P) and voltage sensors (LV-25P) are utilized for the closed loop feedback signals to the microcontroller. The estimated values of the resistance and reactance under balanced grid voltage conditions are presented in Figure 20. The estimated value of the resistance is a bit higher than the dc resistance of the inductor. This can be attributed to the inverter bridge conduction and switching losses, and the winding resistances. Figure 21 shows that the proposed estimation technique also gives the values of the resistance and reactance under unbalanced grid voltage conditions. During unbalanced grid voltage conditions, the positive sequence estimated resistance and reactance values are obtained, which for a three-phase three-wire system are the same. Figure 22 presents the transient performance of the proposed estimation technique during a current transient similar to simulation. The estimated resistance and reactance drop with increase in current, which can be attributed to the respectively due to nonlinear variations of the IGBT module resistance and the drop in estimated reactance can be attributed to saturation of the inductor core. Such a phenomenon is not observed in simulation studies as in that case the RL filter is considered to be linear and the IGBTs are taken to be ideal. Similarly, Figure 23 presents the dynamic performance during a resistance switching similar to simulation. Figure 24 illustrates that with the estimation disabled, if the resistance estimate is different than the actual there is a steady state error between the reference and the actual current. As soon as the estimation is enabled, the actual current tracks the reference without any steady-state error. Similar to Figure 19, the same result is obtained experimentally and is presented in Figure 25.

Figure 22 indicates that when there is a transient in current, both the estimated resistance and reactance reduce in value. This can be attributed to the fact of nonlinear variation of equivalent resistance of the inverter module and the line reactor. In the datasheet of the inverter module, BSM30GP60, the relationship between I_c vs V_{CE} is shown to be nonlinear. As the proposed estimation technique presents the equivalent series resistance from the inverter to the grid, therefore as the current increases, the estimated resistance changes. From the datasheet two values of collector currents and collector emitter voltages are chosen to show how the equivalent nonlinear resistance changes with the increase in the current:

$$\begin{aligned} I_{c1} &= 1A, V_{CE1} = 0.6\ V \\ I_{c2} &= 5A, V_{CE2} = 1\ V \end{aligned} \tag{34}$$

Considering the power losses in the two cases, let the equivalent resistances be marked as R_1 and R_2 respectively for the two chosen currents. Therefore we can write;

$$\begin{aligned} R_1 &= \tfrac{1\times 0.6}{1^2} = 0.6\ \Omega \\ R_2 &= \tfrac{5\times 1}{5^2} = 0.2\ \Omega \end{aligned} \tag{35}$$

Clearly from (34) and (35), an increase in the current through the inverter results in a reduction of the equivalent resistance, as further seen in Figure 22. Also for the estimated reactance the reduction in the equivalent estimated reactance can be attributed to the fact that with increase in the current flowing, the interfacing reactance is partially saturated and the overall reactance of system is reduced. A similar verification using numerical values can be obtained like the equivalent resistance from the datasheet of the reactor (RL-01203 from MTE).

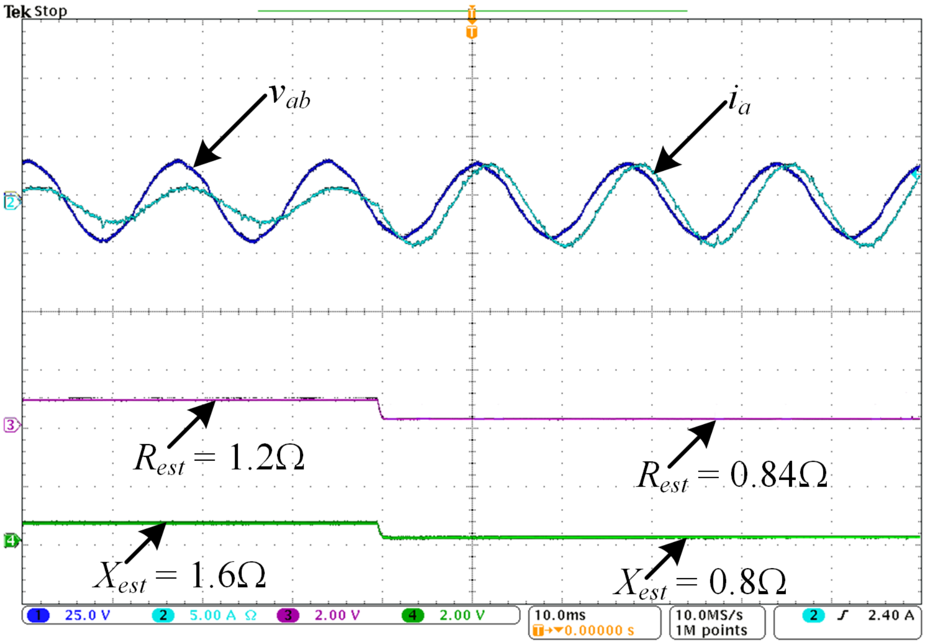

Figure 22. Performance of the controller during a line current transition (R_{est} : 0.6 Ω/div, X_{est} : 1.5 Ω/div)

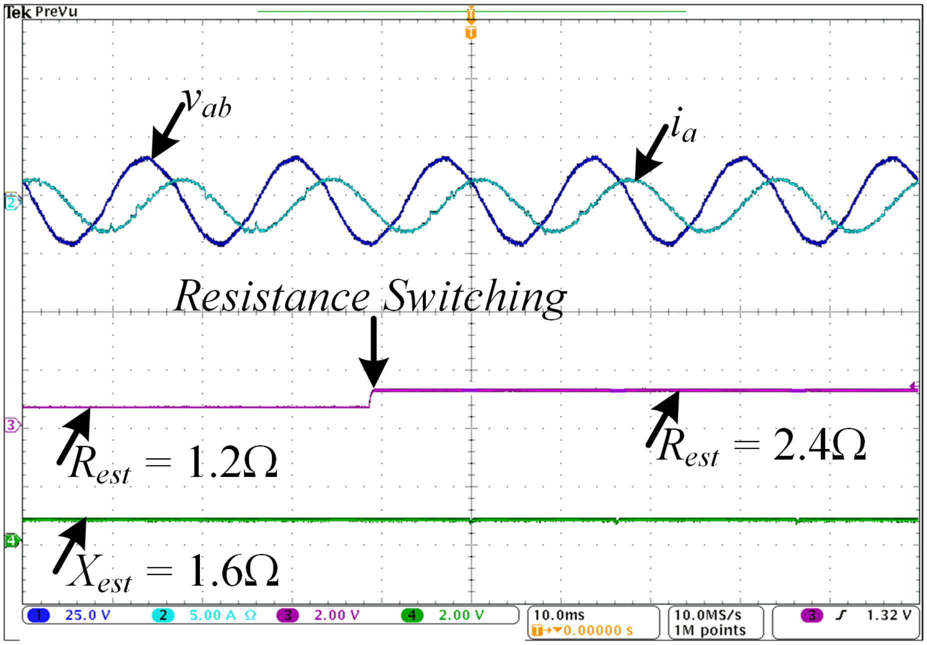

Figure 23. Line voltage and line current during addition of a resistance equal to the nominal value of the RL (R_{est} : 0.6 Ω/div, X_{est} : 1.5 Ω/div)

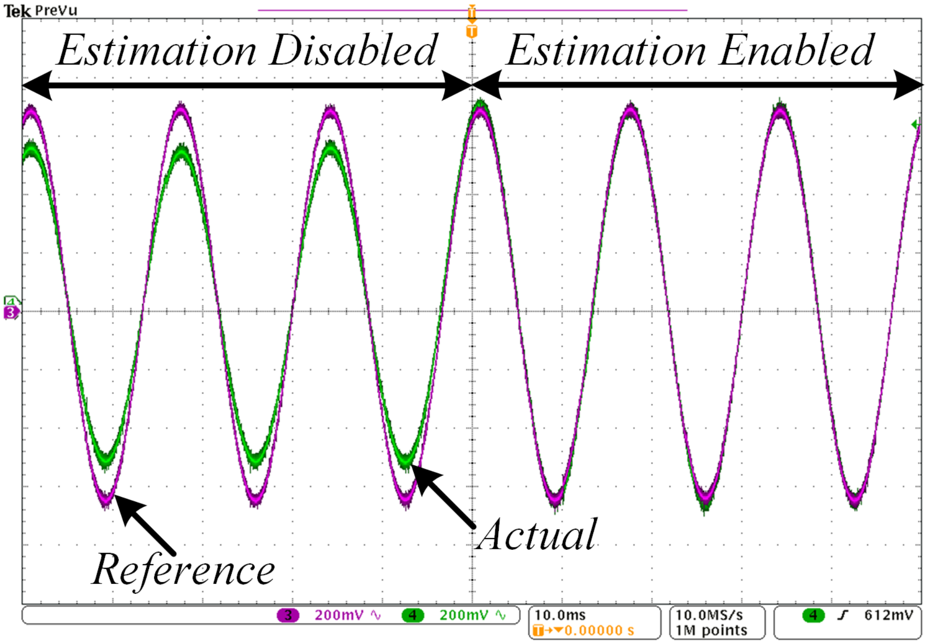

Figure 24. Line current reference and actual with and without the estimation (I_{ref}/I_{actual} : $0.2\ A/div$)

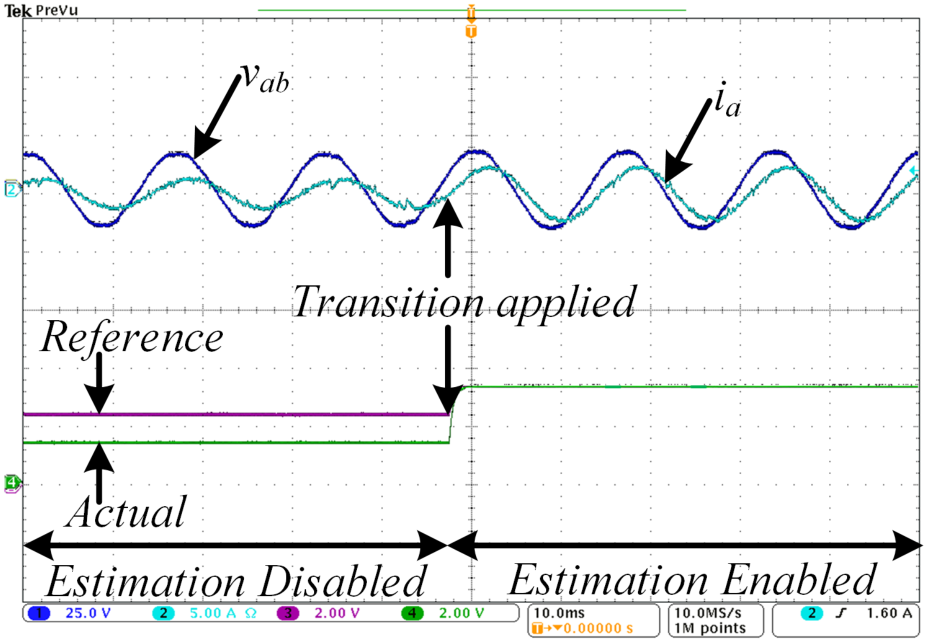

Figure 25. Transient in current and estimation enabling at the same time in a virtual dq frame from experiment (I_{ref}/I_{actual} : $0.2\ A/div$)

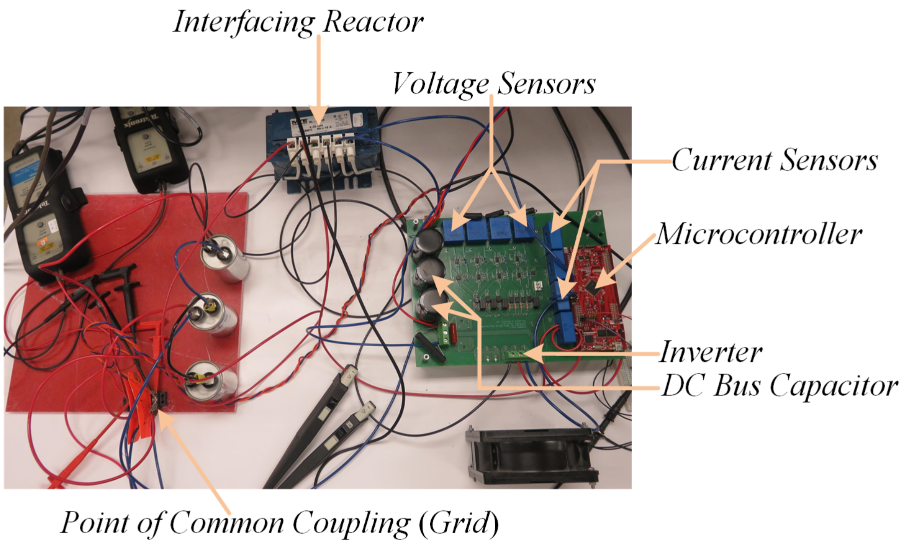

Figure 26. Picture of the experimental setup

6. CONCLUSION

A new estimation technique for the extraction of equivalent resistance and reactance for a three-phase grid connected inverter with RL filter has been proposed in this paper. It has been presented that with the proposed estimation technique, it is possible to online monitor the equivalent impedance and adaptively change the plant parameters. The performance is verified via computer simulations, and various case study results are presented. The proposed estimation technique has also been verified on a reduced-scale laboratory prototype, and the performance is verified. The estimation technique presented in this paper shows stable performance when applied to a parameter-dependent control architecture.

BIBLIOGRAPHY

[1] M. P. Kazmierkowski and L. Malesani, "Current control techniques for three-phase voltage-source PWM converters: A survey," *IEEE Transactions on Industrial Electronics*, vol. 45, pp. 691–703, October 1998.

[2] A. Timbus, M. Liserre, R. Teodorescu, P. Rodriguez, and F. Blaabjerg, Evaluation of current controllers for distributed power generation systems," *IEEE Transactions on Power Electronics*, vol. 24, pp. 654–664, March 2009.

[3] F. Blaabjerg, R. Teodorescu, M. Liserre, , and A. V. Timbus, "Overview of control and grid synchronization for distributed power generation systems,"*IEEE Transactions on Industrial Electronics*, vol. 53, pp. 1398–1409, October 2006.

[4] V. Blasko and V. Kaura, "A new mathematical model and control of a three phase acdc voltage source converter," *IEEE Transactions on Power Electronics*, vol. 12, pp. 116–123, January 1997.

[5] D. G. Holmes, T. A. Lipo, B. P. McGrath, and W. Y. Kong, "Optimized design of stationary frame three phase ac current regulators," *IEEE Transactions on Power Electronics*, vol. 24, pp. 2417–2426, November 2009.

[6] J. Dannehl, F. W. Fuchs, and P. B. Thogersen, "PI state space current control of grid-connected PWM converters with LCL filters," *IEEE Transactions on Power Electronics*, vol. 25, pp. 2320–2330, September 2010.

[7] J. Rodriguez *et al.*,"Predictive current control of a voltage source inverter," *IEEE Transactions on Industrial Electronics*, vol. 54, pp. 495–503, February 2007.

[8] S. Kouro, R. V. P. Cortes, U. Ammann, and J. Rodriguez, "Model predictive control–a simple and powerful method to control power converters,"*IEEE Transactions on Industrial Electronics*, vol. 56, pp. 1826–1838, June 2009.

[9] J. M. Espi, J. Castello, R. Garcia-Gil, G. Garcera, and E. Figueres, "An adaptive robust predictive current control for three-phase grid-connected inverters," *IEEE Transactions on Industrial Electronics*, vol. 58, pp. 3537–3546, August 2011.

[10] Y. A.-R. I. Mohamed and E. F. El-Saadany,"Adaptive discrete-time grid-voltage sensorless interfacing scheme for grid-connected dg-inverters based on neural-network identification and deadbeat current regulation," *IEEE Transactions on Power Electronics*, vol. 23, pp. 308–321, January 2008.

[11] Y. A.-R. I. Mohamed, E. F. El-Saadany, and M. M. A. Salama, "Adaptive grid-voltage sensorless control scheme for inverter-based distributed generation," *IEEE Transactions on Energy Conversion*, vol. 24, pp. 683–694, September 2009.

[12] A. Vidal, A. G. Yepes, F. D. Freijedo, J. Malvar, O. Lopez, and J. Doval-Gandoy, "A technique to estimate the equivalent loss resistance of grid-tied converters for current control analysis and design," *IEEE Transactions on Power Electronics*, vol. 30, pp. 1747–1761, March 2015.

[13] A. Vidal *et al.*, "A method for identification of the equivalent inductance and resistance in the plant model of current-controlled grid-tied converters," *IEEE Transactions on Power Electronics*, vol. 30, pp. 7245–7261, December 2015.

[14] S. Maiti, C. Chakraborty, Y. Hori, and M. C. Ta, "Model reference adaptive controller-based rotor resistance and speed estimation techniques for vector controlled induction motor drive utilizing reactive power," *IEEE Transactions on Industrial Electronics*, vol. 55, pp. 594–601, February 2008.

[15] A. V. R. Teja, C. Chakraborty, S. Maiti, and Y. Hori, "A new model reference adaptive controller for four quadrant vector controlled induction motor drives," *IEEE Transactions on Industrial Electronics*, vol. 59, pp. 3757–3767, October 2012.

[16] C. Schauder, "Adaptive speed identification for vector control of induction motors without rotational transducers," *IEEE Transactions on Industry Application*, vol. 28, pp. 1054–1061, October 1992.

[17] L. Zhen and L. Xu, "Sensorless field orientation control of induction machines based on a mutual MRAS scheme," *IEEE Transactions on Industrial Electronics*, vol. 45, pp. 824–831, October 1998.

[18] V. Vasic, S. N. Vukosavic, and E. Levi, "A stator resistance estimation scheme for speed sensorless rotor flux oriented induction motor drives," *IEEE Transactions on Energy Conversion*, vol. 18, pp. 476–483, December 2003.

[19] R. Cardenas and R. Pena, "Sensorless vector control of induction machines for variable-speed wind energy applications," *IEEE Transactions on Energy Conversion*, vol. 19, pp. 196–205, March 2004.

[20] R. Cardenas, R. Pena, J. Proboste, G. Asher, and J. Clare, "MRAS observer for sensorless control of standalone doubly fed induction generators,"*IEEE Transactions on Energy Conversion*, vol. 20, pp. 710–718, December 2005.

[21] R. Cardenas, R. Pena, G. Asher, J. Clare, and J. Cartes, "MRAS observer for doubly fed induction machines," *IEEE Transactions on Energy Conversion*, vol. 19, pp. 467–468, June 2004.

[22] R. Pena, R. Cardenas, J. Proboste, G. Asher, and J. Clare, "Sensorless control of doubly-fed induction generators using a rotor-current-based MRAS observer," *IEEE Transactions on Industrial Electronics*, vol. 55, pp. 330–339, January 2008.

[23] R. Cardenas, R. Pena, S. Alepuz, and G. Asher, "Overview of control systems for the operation of DFIGs in wind energy applications," *IEEE Transactions on Industrial Electronics*, vol. 60, pp. 2776–2798, July 2013.

[24] M. Singh and A. Chandra, "Application of adaptive network-based fuzzy inference system for sensorless control of PMSG-based wind turbine with nonlinear-load-compensation capabilities," *IEEE Transactions on Power Electronics*, vol. 26, pp. 165–175, January 2011.

[25] M. Rashed, F. A. Peter, A. MacConnell, A. F. Stronach, and P. Acarnley, “Sensorless indirect-rotor-field-orientation speed control of a permanent magnet synchronous motor with stator-resistance estimation,” *IEEE Transactions on Industrial Electronics*, vol. 54, pp. 1664–1675, June 2007.

[26] P. Rodriguez, R. Teodorescu, I. Candela, A. V. Timbus, M. Liserre, and F. Blaabjerg., “New positive-sequence voltage detector for grid synchronization of power converters under faulty grid conditions,” in *Proc. 37th Annual IEEE Power Electronics Specialist Conf.*, Jeju, South Korea, June 2006.

[27] P. Rodriguez, A. Luna, M. Ciobotaru, R. Teodorescu, and F. Blaabjerg, “Advanced grid synchronization system for power converters under unbalanced and distorted operating conditions,” in *Proc. 32nd IEEE-IECON.*, Paris, France, November 2006, pp. 5173–5178.

[28] P. Rodriguez, A. Luna, I. Candela, R. Mujal, R. Teodorescu, and F. Blaabjerg, “Multiresonant frequency-locked loop for grid synchronization of power converters under distorted grid conditions,” *IEEE Transactions on Industrial Electronics*, vol. 58, pp. 127–138, January 2011.

[29] H. Komurcugil, N. Altin, S. Ozdemir, and I. Sefa, “Lyapunov-function and proportional-resonant-based control strategy for single-phase grid-connected VSI with LCL filter,” *IEEE Transactions on Industrial Electronics*, vol. 63, pp. 2838–2849, May 2016.

[30] V. R. Chowdhury, S. Mukherjee, and J. Kimball, “A voltage sensorless control of a three phase grid connected inverter based on Lyapunov energy function under unbalanced grid voltage condition,” in *Proc. 10th IEEE Energy Conversion Congress and Exposition*, Portland, USA, September 2018.

II. GRID VOLTAGE SENSORLESS SYNCHRONIZATION OF A THREE PHASE GRID CONNECTED INVERTER UNDER UNBALANCED GRID VOLTAGE CONDITION

ABSTRACT

Grid connected inverters require accurate knowledge of the grid voltage for the generation of unit vectors from phase locked loops (PLL). However, when the grid voltage sensor fails or the grid is physically far from the point of common coupling (PCC), it is not possible to continue to run the inverter and thereby a shut down becomes the only option. In this paper, a new globally stable passive grid voltage estimation architecture has been proposed based on the internal model principle. The proposed control architecture relies on the current sensors and filter parameters (RL from inverter to the grid) for the grid voltage estimation and generates the phase locked loop information. Detailed sensitivity analysis is presented to show that the proposed estimation scheme for the grid voltage is practically insensitive to parameter variations. In comparison to conventional current control with both grid voltage and current sensors, the proposed current control scheme provides better transient response during both ideal and non-ideal grid voltage conditions. Simulation based on MATLAB/Simulink and PLECS and experimental results validate the efficacy of the proposed control come estimation technique discussed in this paper.

1. INTRODUCTION

Environmental issues and energy crises have led to the usage of renewable energy resources more and more aggressively in recent times [1–3]. Therefore, controlling grid connected inverters interfacing these renewables optimally is a necessity. The most widespread control architecture for a grid-connected inverters is the current-controlled architecture which separately controls the active and reactive power supplied from the inverter to the grid. The controllers for current control architecture are designed to achieve desired performance for the system depending on small signal modeling of the plant [4,5,7], which limits large-signal response capability. A current-control architecture requires accurate information for the grid voltage to generate the frequency and the phase information through a phase locked loop (PLL), a highly active area of research [8,9,12]. However, existing PLL methods require accurate grid voltage information. Other popular approaches similar to current control, like model predictive control (MPC) [13,14] also need this grid voltage information.

Recently, control architectures for a three phase grid connected inverter based on Lyapunov energy function have been studied. The present work builds on previous methods [16,17,19] and eliminates the need for grid voltage sensors by incorporating a novel grid voltage estimation technique based on the internal model principle. Grid voltage sensors can be large, expensive, and susceptible to faults, so their elimination reduces cost and size while improving robustness.

Previously reported methods provide useful comparisons but each has deficiencies. The method in [17] is only for a single-phase, standalone system (no grid connection). The method in [16] addresses an inverter with LCL filter by adding a proportional resonant (PR) controller. However, voltage sensors are needed for resonance damping. The method in [19] has the same sensor requirements and adds a PLL to enable control in a synchronous dq frame.

Estimation of grid voltage for grid-connected inverters has also been reported in [20, 21]. However, the methodology reported in [20] is only applicable during unity power factor operation. The reported architecture described in [21] requires a derivative operation, which increases the noise for the overall estimation architecture. Other methodologies presented in [22,24,25] use virtual flux, which relies on integration. A pure integrator suffers from dc drift. Therefore, for the implementation, a low-pass filter is used instead, which introduces gain and phase errors. Also, virtual flux methods neglect resistive drop in the inductors used for grid connection, which is sometimes significant, as well as the equivalent resistive drop due to the overall losses in the system.

Internal model-based controllers have been reported in the literature [26, 27]. This methodology relies on the fact that an internal model of the plant based on its nominal values is embedded inside the controller architecture and the outputs from them are measured. These outputs are compared with the actual outputs, and the error between them is processed through a compensator to generate control input. Detailed system modeling along with the controller architecture derivation has been presented. System modeling and derivation of the internal model-based grid voltage estimation architecture has also been presented. Simulation results based on MATLAB/Simulink[1] and PLECS[2] are validated with a reduced-scale laboratory prototype. Detailed sensitivity analysis illustrates the accuracy of the voltage estimation algorithm.

The rest of the paper is organized as follows: Section 2 introduces the voltage estimation technique, with gain selection criteria and sensitivity analysis. Section 3 presents the verification of the proposed estimation technique along with a known current control architecture on a three phase grid connected inverter. Section 4 provides verification with simulation and experiments, and Section 5 concludes the work.

2. GRID VOLTAGE ESTIMATION

2.1. INTERNAL MODEL BASED GRID VOLTAGE ESTIMATION WITH PASSIVITY BASED ANALYSIS

A novel internal model based grid voltage estimation technique is presented in this subsection. The basic structure of an internal model based architecture contains the nominal plant model embedded within the controller. The error between the actual plant output and

---

[1] MATLAB and Simulink are registered trademarks of The MathWorks, Inc.

[2] PLECS is a registered trademark of Plexim GmbH.

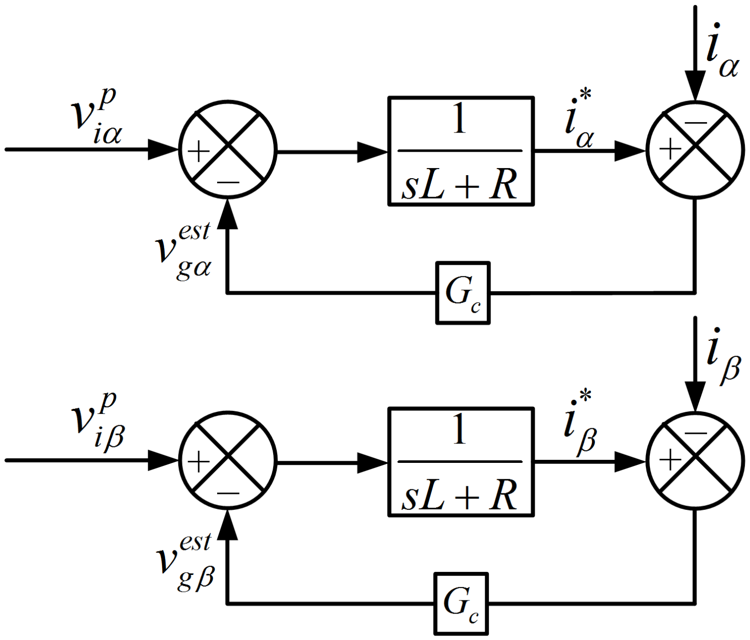

Figure 1. Simplified block diagram for the grid voltage estimator

the internal model output drives the system. The simplified block diagram for the grid voltage estimator based on this architecture is presented in Figure 1 where $v_{i\alpha}^{p}$ and $v_{i\beta}^{p}$ are the positive sequence inverter voltages obtained from the output of the Lyapunov based current controller using a DSOGI; i_α and i_β are the sensed currents from the inverter; i_α^* and i_β^* are the currents from the internal model of the plant embedded inside the estimator structure; and G_c is the compensator.

For the block diagram of Figure 1, the inputs are the instantaneous positive sequence inverter voltages, $v_{i\alpha}^{p}$ and $v_{i\beta}^{p}$, which are sinusoidal in nature. Therefore, the compensator G_c is chosen as a proportional resonant (PR) controller [2],

$$G_c = K_p + \frac{2\omega_{cut}K_r s}{s^2 + 2\omega_{cut}s + \omega^2}, \tag{1}$$

where ω_{cut} is the attenuation frequency, K_p and K_r are the gains of the resonant controller, and ω is the operating frequency.

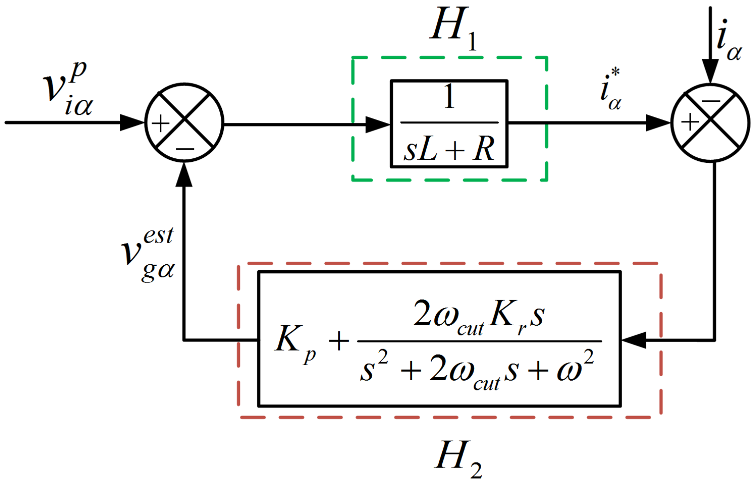

Figure 2. Simplified block diagram of grid voltage estimator with all the subsystems

The well-known concept of passivity may be used to prove estimator convergence. Feedback connection of two passive systems is passive [32]. Figure 1 has been redrawn in Figure 2 for only the α axis considering symmetry with the two subsystems presented as H_1 and H_2 for the internal model and the compensator, respectively. Consider now the subsystem marked as H_1 in Figure 2. A state space model of H_1 is given by

$$\begin{aligned} \dot{x} &= -\frac{R}{L}x + \frac{1}{L}u \\ y &= x \end{aligned} \tag{2}$$

where $y = x = i_\alpha^*$, $u = v_{i\alpha}^{p} - v_{g\alpha}^{est}$. Let us consider a Lyapunov function for (2) given by

$$V_{H_1} = \frac{1}{2}Lx^2 \tag{3}$$

Differentiating (3) with respect to time and using (2), we have

$$\dot{V}_{H_1} = -Rx^2 + ux \tag{4}$$

Therefore from (4) it can be concluded that

$$uy = ux \geq \dot{V}_{H_1} \tag{5}$$

implying that the system H_1 (i.e. the plant) is passive. Similarly, let us proceed for the system H_2 (i.e. the compensator). A state space model of the compensator in controllable canonical form [32] is given by

$$\begin{aligned} \begin{bmatrix} \dot{x}_1 \\ \dot{x}_2 \end{bmatrix} &= \begin{bmatrix} 0 & 1 \\ -\omega^2 & -2\omega_{cut} \end{bmatrix} \begin{bmatrix} x_1 \\ x_2 \end{bmatrix} + \begin{bmatrix} 0 \\ 1 \end{bmatrix} v \\ y &= \begin{bmatrix} 0 & 2\omega_{cut}K_r \end{bmatrix} \begin{bmatrix} x_1 \\ x_2 \end{bmatrix} + K_p v \end{aligned} \tag{6}$$

where $v = i_\alpha^* - i_\alpha$. Let us consider another Lyapunov energy function for the system H_2 given by

$$V_{H_2} = \frac{1}{2}ax_1^2 + \frac{1}{2}bx_2^2 \tag{7}$$

where a and b are greater than zero and are defined by $a = \frac{2\omega_{cut}K_r}{\omega^2}$ and $b = 2\omega_{cut}K_r$. Differentiating (7) with respect to time and using (6), we have

$$\dot{V}_{H_2} = -4\omega_{cut}^2 K_r x_2^2 - K_p u^2 + vy \tag{8}$$

Similar to (5), it can be concluded from (8) that

$$vy \geq \dot{V}_{H_2} \tag{9}$$

which implies that the system H_2 (i.e. the compensator) is also passive. Since a feedback connection of two passive systems (here H_1 and H_2) is passive, the overall grid voltage estimator is passive and therefore globally asymptotically stable. The next subsection analyzes the small-signal characteristics to assist in choosing the compensator gains.

2.2. SMALL-SIGNAL MODELLING OF THE PROPOSED INTERNAL MODEL-BASED GRID VOLTAGE ESTIMATOR

From the proposed structure of the internal model-based grid voltage estimator presented in Figure 2, the system H_1 may be written as

$$V_{i\alpha}^{pref}(s) = sLI_\alpha^*(s) + RI_\alpha^*(s) + V_{g\alpha}^{est}(s) \tag{10}$$

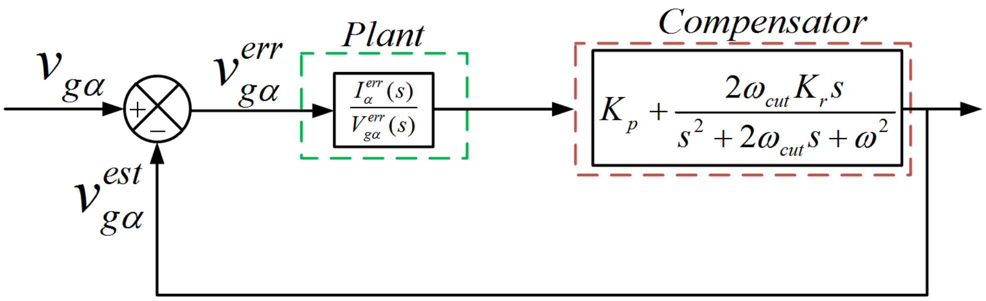

Figure 3. Small signal block diagram of the grid voltage estimator

where $V_{i\alpha}^{pref}(s)$ is the output voltage from the Lyapunov-based current controller, $I_{\alpha}^{*}(s)$ is the current output from the internal model of the plant (i.e. the RL filter from the inverter to the grid in this case) and $V_{g\alpha}^{est}(s)$ is the estimated grid voltage, all in Laplace domain. Similarly to (10), the KVL equation of the inverter to the grid considering fundamental positive sequence voltage is given by

$$V_{i\alpha}^{p}(s) = sLI_{\alpha}(s) + RI_{\alpha}(s) + V_{g\alpha}(s) \tag{11}$$

where $V_{i\alpha}^{p}(s)$ is the fundamental component of the inverter voltage, $I_{\alpha}(s)$ is the inverter current and $V_{g\alpha}(s)$ is the grid voltage all in Laplace domain. Now let us define few quantities as $I_{\alpha}^{err}(s) = I_{\alpha}^{*}(s) - I_{\alpha}(s)$ and $V_{g\alpha}^{err}(s) = V_{g\alpha}(s) - V_{g\alpha}^{est}(s)$. Taking a difference of (11) from (10), we have

$$V_{i\alpha}^{pref}(s) - V_{i\alpha}^{p}(s) = (sL + R)I_{\alpha}^{err}(s) - V_{g\alpha}^{err}(s) \tag{12}$$

Considering the current controller dynamics to be much faster than the estimator dynamics we can write $V_{i\alpha}^{pref}(s) = V_{i\alpha}^{p}(s)$ in (12). As a result, the left-hand side of (12) becomes equal to zero. Therefore, the small-signal transfer function of the current error to the error in the estimated grid voltage becomes

$$\frac{I_{\alpha}^{err}(s)}{V_{g\alpha}^{err}(s)} = \frac{1}{sL + R} \tag{13}$$

Equation (13) can be represented in a simplified block diagram format as presented in Figure 3 with the compensator block included. The frequency response of the estimator

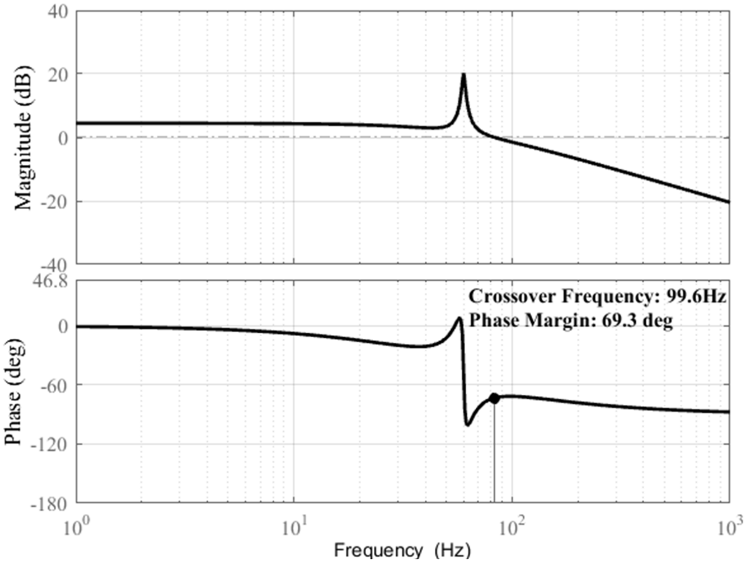

Figure 4. Frequency response of the open loop gain for grid voltage estimator

Table 1. Plant and Compensator Parameters

Parameter	**Value**
L	4.2 mH
R	1.15 Ω
K_p	2 A/V
K_r	80 A/V
ω_{cut}	5 rad/s
f_s	20 kHz
k	1.2

(i.e. the Bode plot from the small-signal model) is presented in Figure 4. The plant parameter and chosen compensator parameters are presented in Table 1. The Bode plot of Figure 4 indicates that the bandwidth of the estimator is kept approximately two decades lower than the switching frequency f_s. The next subsection presents the sensitivity of the estimated grid voltage to the variation of plant parameters (i.e. R and L of the interfacing reactor from the inverter to the grid).

2.3. PARAMETER SENSITIVITY ANALYSIS AND ITS EFFECT ON ESTIMATED GRID VOLTAGE

The estimated grid voltage is dependent on the plant parameters (i.e. R and L of the interfacing reactance from the inverter to the grid). In practical situations, the plant parameters are not exactly known and vary with their operation. To show the effect of parameter variations, the system dynamic model is carried out in a fictitious synchronous dq frame of reference (not used in actual implementation). In steady state, the inverter voltage, grid voltage and the current are related as

$$\begin{aligned} V_{id}^{fund} &= RI_{d}^{fund} - \omega LI_{q}^{fund} + V_{gd}^{fund} \\ V_{iq}^{fund} &= RI_{q}^{fund} + \omega LI_{d}^{fund} + V_{gq}^{fund} \end{aligned} \tag{14}$$

where the superscript '$fund$' denotes fundamental component. Considering the Lyapunov-based current controller to be much faster (at least a decade higher bandwidth) than the estimator, the estimated grid voltage, the current and the inverter voltage are related as

$$\begin{aligned} V_{id}^{fund} &= R_{nom}I_{d}^{fund} - \omega L_{nom}I_{q}^{fund} + V_{gdest}^{fund} \\ V_{iq}^{fund} &= R_{nom}I_{q}^{fund} + \omega L_{nom}I_{d}^{fund} + V_{gqest}^{fund} \end{aligned} \tag{15}$$

where R_{nom} and L_{nom} are the nominal values of the plant parameters (i.e. the interfacing reactance between the inverter to the grid).

Define $R_{err} = R - R_{nom}$, $L_{err} = L - L_{nom}$ and $V_{gpk}^{fund} = \sqrt{\left(V_{gd}^{fund}\right)^2 + \left(V_{gq}^{fund}\right)^2}$. If the d axis of the estimated voltage is latched with the estimated voltage phasor then $V_{gdest}^{fund} = V_{gest}^{fund}$ and $V_{gqest}^{fund} = 0$. Subtracting (15) from (14), the relation between the error in the estimated voltage is

$$\begin{aligned} V_{gd}^{fund} &= V_{gest}^{fund} - R_{err}I_{d}^{fund} + \omega L_{err}I_{q}^{fund} \\ V_{gq}^{fund} &= -R_{err}I_{q}^{fund} - \omega L_{err}I_{d}^{fund} \end{aligned} \tag{16}$$

From (16), we have

$$\left(V_{gpk}^{fund}\right)^2 = \left(V_{gest}^{fund} - R_{err}I_{d}^{fund} + \omega L_{err}I_{q}^{fund}\right)^2 + \left(-R_{err}I_{q}^{fund} - \omega L_{err}I_{d}^{fund}\right)^2 \tag{17}$$

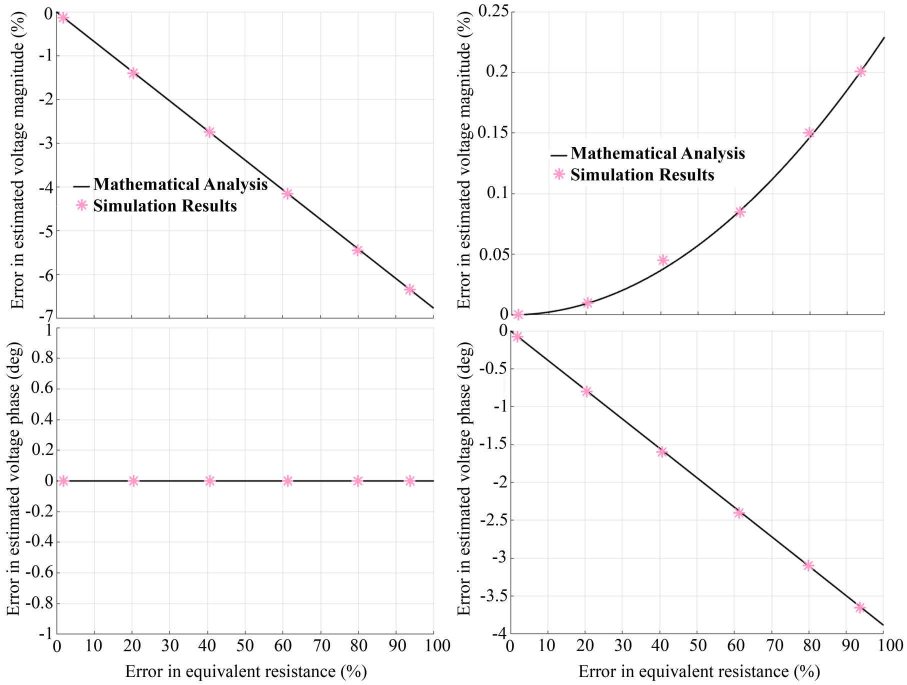

Figure 5. Error in magnitude and phase of estimated grid voltage with variation of resistance and inductance while supplying rated active power

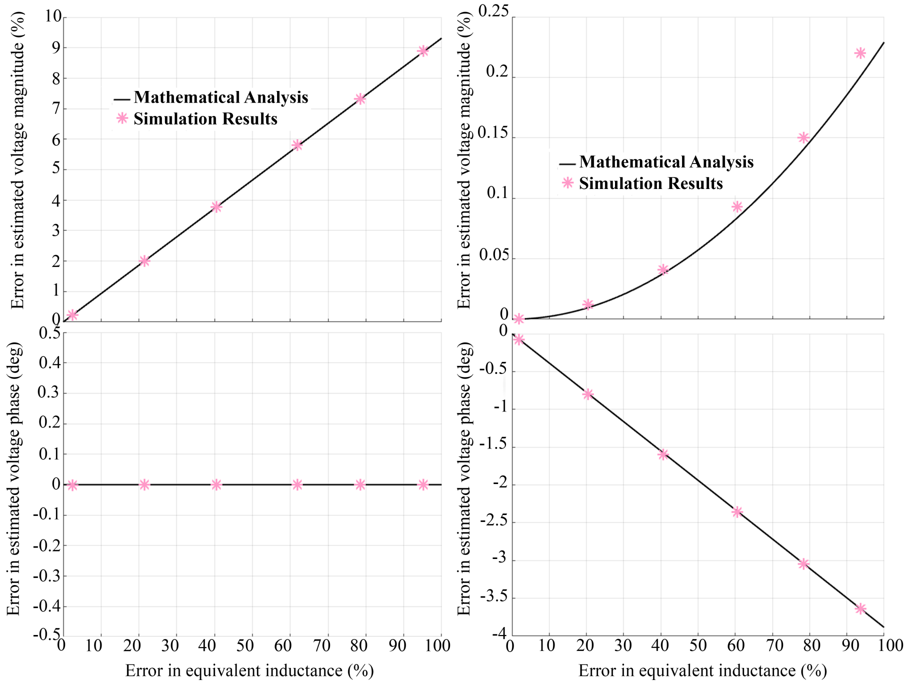

Figure 6. Error in magnitude and phase of estimated grid voltage with variation of resistance and inductance while supplying rated reactive power

Equation (17) is solved to find the magnitude of the estimated voltage V_{gest}^{fund}. Then, the percentage error is calculated from the actual grid voltage by considering a 100% variation in plant parameters R and L. The percentage error in magnitude is given by

$$V_{gesterr(\%)}^{fund} = \left(\frac{V_{gpk}^{fund} - V_{gest}^{fund}}{V_{gest}^{fund}} \right) \times 100 \tag{18}$$

The calculated V_{gd}^{fund} and V_{gq}^{fund} from (16) is utilized to find the error in the phase angle of the estimated grid voltage which is related as

$$\theta_{err} = \tan^{-1} \left(\frac{V_{gq}^{fund}}{V_{gd}^{fund}} \right) \tag{19}$$

Figures 5 and 6 illustrate numerical solutions to (18) and (19), compared to the estimated grid voltage from the simulation in MATLAB/Simulink and PLECS for operation at rated active and reactive power, respectively. These results indicate that the Lyapunov energy function-based controller can work satisfactorily with proper generation of the unit vectors even with significant variation in component parameters. Some small errors remain (less than 5% in both magnitude and phase). However, for cases when there can be failure in the grid voltage sensing or the *PCC* is physically far from the inverter, such a methodology can help to maintain seamless operation of the converter without a shut down.

The proposed grid voltage estimation technique relies on the nominal values of the interfacing reactance R and L. To check the efficacy of the proposed sensorless scheme, a current control architecture based on Lyapunov energy function is considered as presented in [16]. The next section briefly explains the current control architecture.

3. CONTROL ARCHITECTURE

In this section, Lyapunov energy function based current control architecture introduced in [16] is applied with the proposed grid voltage sensorless scheme presented in the previous section. The basic governing equation for the modulation indices obtained from a

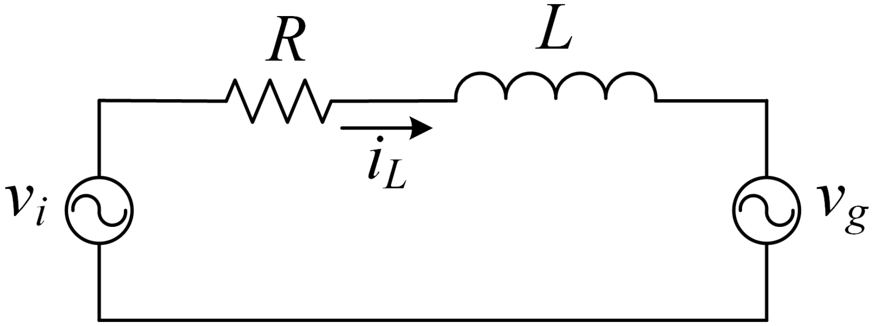

Figure 7. Equivalent circuit of a three phase grid connected inverter with RL filter

Lyapunov energy function as detailed out in [16, 17] are given in $\alpha\beta$ domain by:

$$\begin{aligned} m^*_\alpha + \Delta m_\alpha &= \tfrac{2}{V_{dc}}\left(L\tfrac{di^*_\alpha}{dt} + i^*_\alpha R + v_{g\alpha}\right) - \tfrac{2R_c}{V_{dc}}x_\alpha \\ m^*_\beta + \Delta m_\beta &= \tfrac{2}{V_{dc}}\left(L\tfrac{di^*_\beta}{dt} + i^*_\beta R + v_{g\beta}\right) - \tfrac{2R_c}{V_{dc}}x_\beta \end{aligned} \tag{20}$$

where $x_\alpha = i_\alpha$ - i^*_α and $x_\beta = i_\beta$ - i^*_β. Using these control laws, the results for the operation of a three-phase grid-connected inverter are presented for various case studies. The value of R_c chosen for the modulation index as shown in (20) is 70. From the Lyapunov-based control strategy presented in [16] and [35], it can be shown that the value of R_c chosen ensures global asymptotic stability of the system. However, in [16, 17, 35], the effect of delay due to sensing and PWM is never considered. In this paper, the overall Lyapunov current control architecture is modified and a criteria for the upper limit of the gain R_c is obtained. A simplified schematic circuit diagram of a three phase grid connected inverter on a per phase basis is presented in Figure 7. Considering symmetry in the circuit, the same circuit can be used for both α and β axes. Considering the fact that the delay due to sensing and PWM can be lumped, the overall closed loop transfer function for the current is obtained as shown:

$$\begin{aligned} sLI_\alpha(s) &= -I_\alpha(s)R + \left(sLI^*_\alpha(s) + I^*_\alpha(s)R + V_{g\alpha}(s)\right) - R_c\left(I_\alpha(s)e^{-1.5sT_{samp}} - I^*_\alpha(s)\right) - V_{g\alpha}(s) \\ sLI_\beta(s) &= -I_\beta(s)R + \left(sLI^*_\beta(s) + I^*_\beta(s)R + V_{g\beta}(s)\right) - R_c\left(I_\beta(s)e^{-1.5sT_{samp}} - I^*_\beta(s)\right) - V_{g\beta}(s) \end{aligned} \tag{21}$$

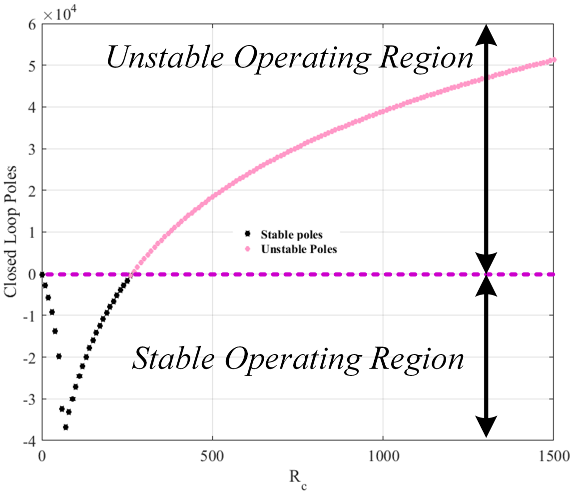

Figure 8. Real part of the closed-loop poles with the variation of R_c considering sampling delay time

where T_{samp} is the sampling time. Generally the sampling time is much lower than the fundamental period (no more than half of the fundamental period, also called Nyquist rate [30]). Simplifying (21), the closed-loop transfer function is given by

$$\begin{aligned} \frac{I_\alpha^*(s)}{I_\alpha(s)} &= \frac{sL + R + R_c}{sL + R + R_c e^{-1.5sT_{samp}}} \\ \frac{I_\beta^*(s)}{I_\beta(s)} &= \frac{sL + R + R_c}{sL + R + R_c e^{-1.5sT_{samp}}} \end{aligned} \tag{22}$$

Utilizing (21), the range of the Lyapunov gain, R_c is obtained by numerically solving for the closed loop poles of (23).

$$f(s) = sL + R + R_c e^{-1.5sT_{samp}} = 0 \tag{23}$$

The location of the closed loop poles showing the stable/unstable boundary is presented in Figure 8. The numerical solution to (23) for a range of R_c is given in Figure 8, using parameter values from Table 1. The switching frequency of the inverter is $f_s = 20\,\text{kHz}$, and with a double update scheme, the sampling frequency becomes $f_{samp} = 40\,\text{kHz}$ and the sampling time period is $T_{samp} = {}^{1}/_{f_{samp}} = 25\,\mu\text{s}$. The next section presents the results and discussions for various case studies with the proposed method. This section presents the verification of the proposed control architecture elaborated in this paper via simulation

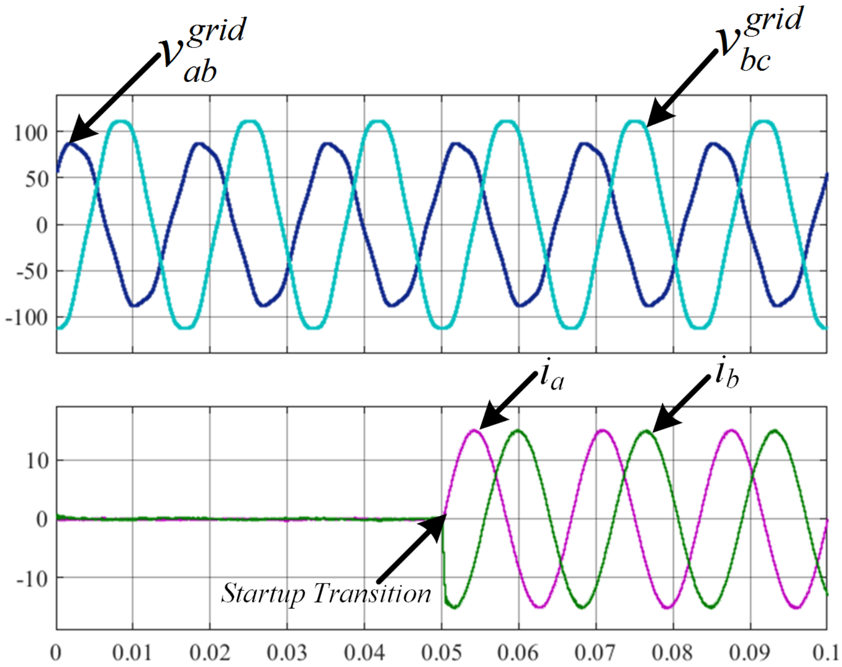

Figure 9. Startup transient of grid current under unbalanced/distorted grid voltage condition from simulation

and experimental studies. The simulation studies were carried out in MATLAB/Simulink and PLECS. The experimental setup was built around a TMS320F28377S microcontroller from Texas Instruments; a BSM30GP60 inverter module from Infineon and LEM Hall-effect current sensors (LA-55P). The parameters of the simulation and experiment are summarized in Table 1. The value of Lyapunov current controller gain R_c is chosen to be equal to 70 V A^{-1} from Figure 8, where the location of the real part of the closed-loop pole is most negative. The proposed architecture is verified via simulation as mentioned earlier and a startup transition result from simulation is presented in Figure 9. A similar result from the experimental study is presented in Figure 10. Clearly, the simulation results are in close agreement with the experimental results. Therefore, only experimental results are presented for the remainder of the cases.

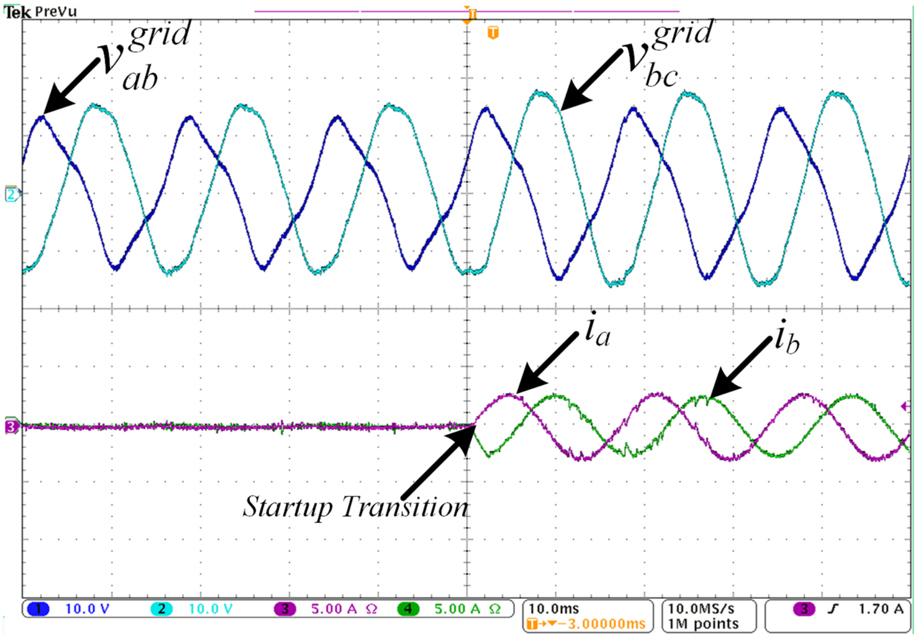

Figure 10. Startup transient of grid current under unbalanced/distorted grid voltage condition from experiment

The effectiveness of the proposed estimation technique and the generation of the unit vectors along with v_{ab} and i_a are presented in Figure 11. The result shows that the proposed estimation technique is able to generate the unit vectors $\sin\theta_{est}$ and $\cos\theta_{est}$ without any distortion. These estimated unit vectors are used for the Lyapunov-based current controller, and successful current control is achieved. Transient results for active power and reactive power steps are given in Figures 12 and 13, respectively. Startup in the rectifier mode is presented in Figure 14. Transient in current from one reference level to the other is presented in Figure 15 for unbalanced/distorted grid condition.

As described in Section 3, the delay due to the sampling time places a bound on the choice of R_c as illustrated in Figure. 8. In Figure. 16 verification of the choice of R_c in stable and unstable zone has been reported. A choice of Lyapunov gain R_c in the unstable zone creates sustained oscillations in the current. Finally, the proposed architecture is compared to the traditional current control architecture described in [18]. Figure 17 presents the verification of the startup transient of current obtained in a virtual dq

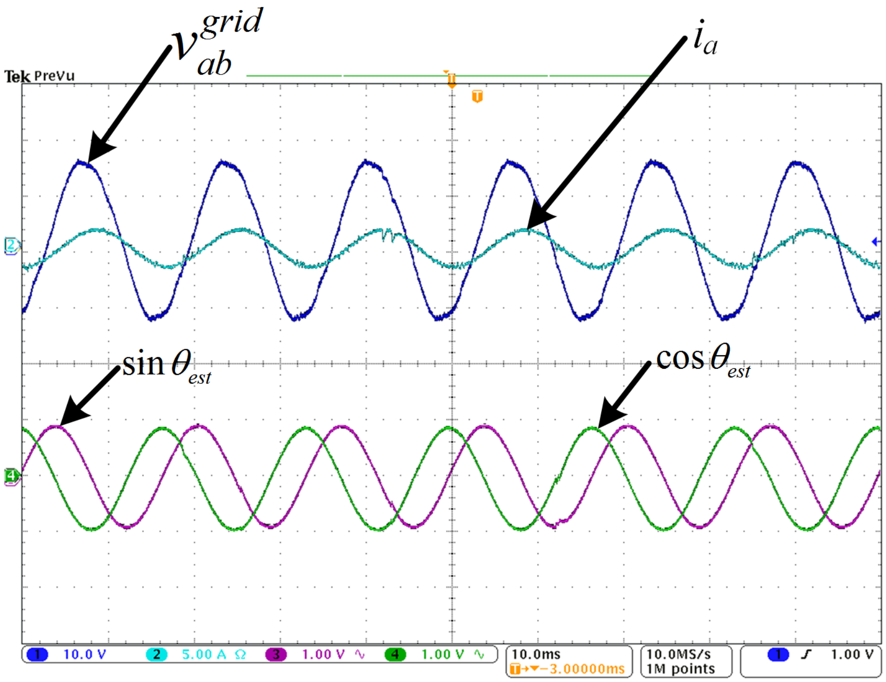

Figure 11. Unit vector generation by the proposed estimation technique from experiment

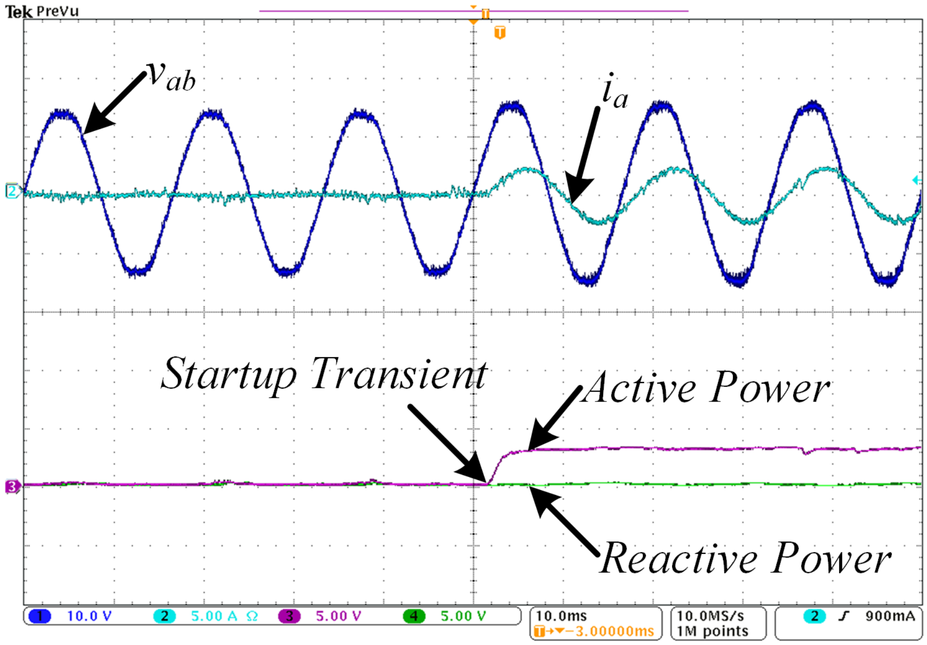

Figure 12. Transient in active power from experiment

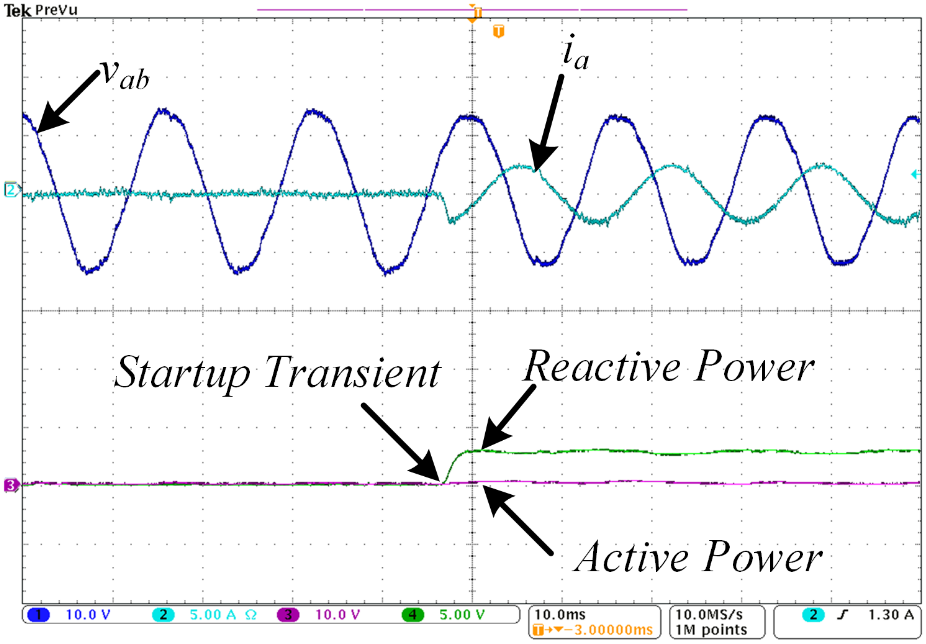

Figure 13. Transient in reactive power from experiment

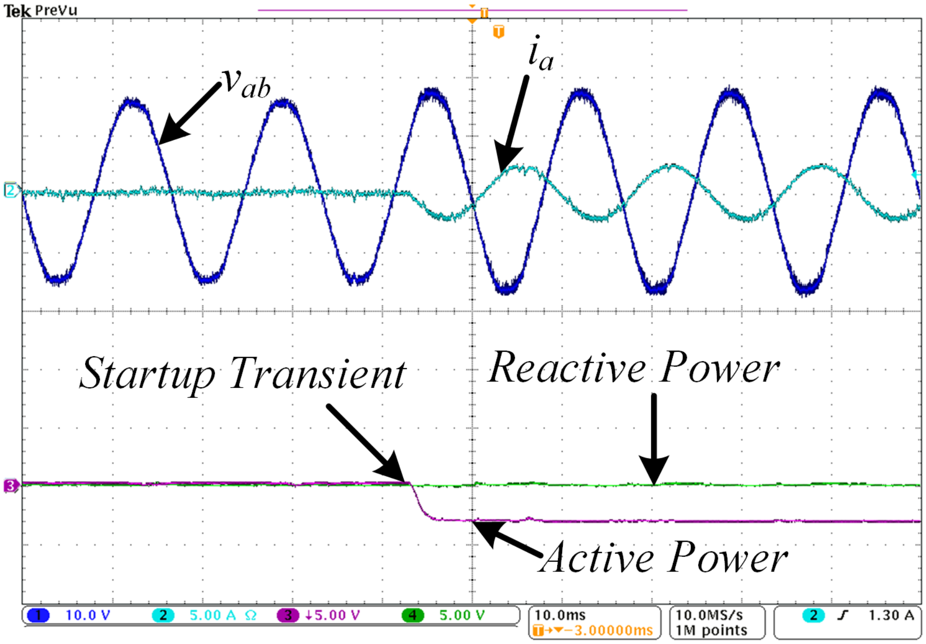

Figure 14. Transient in active power in rectifier mode from experiment

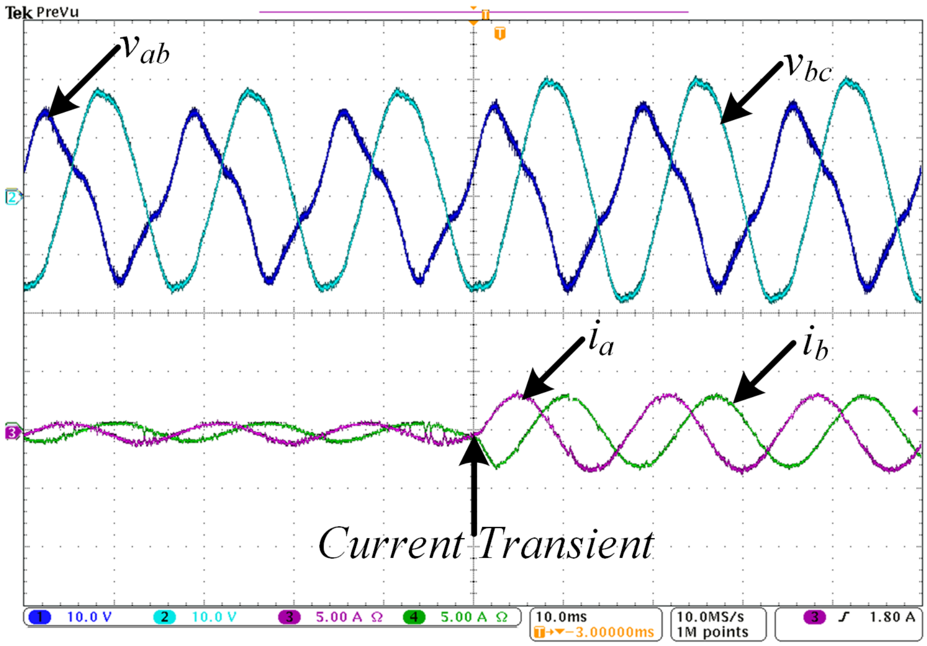

Figure 15. Current transient performance from experiment under unbalanced/distorted grid condition

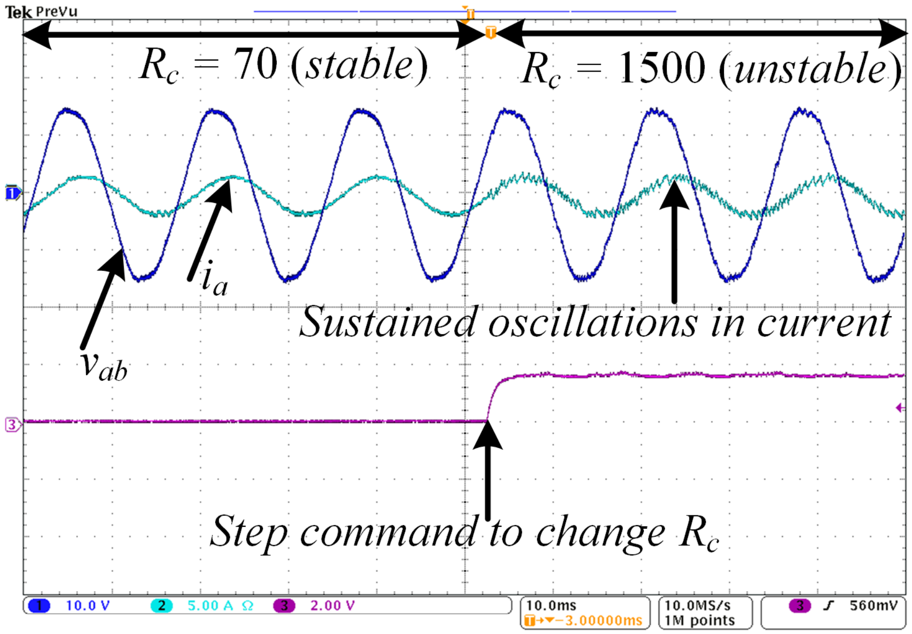

Figure 16. Effect of Lyapunov gain R_c on current from experiment

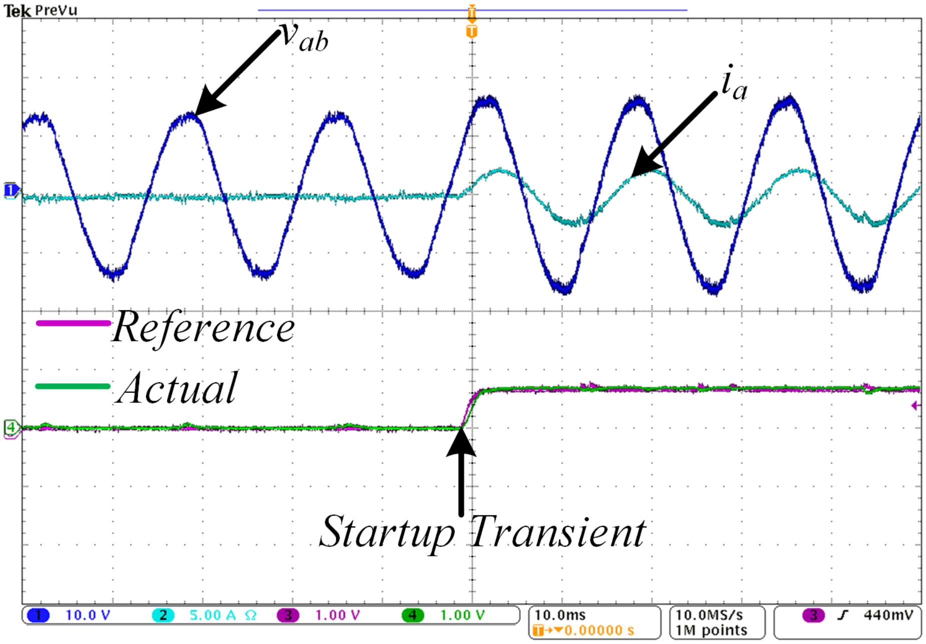

Figure 17. Transient performance of the proposed control architecture in a virtual dq frame from experiment (i_a: 5A/div)

frame of reference with the proposed control architecture. Figure 18 presents verification of startup transient for a traditional current-control architecture with grid voltage sensors. The proposed control architecture achieves a better transient response than the traditional current control architecture. During unbalanced/distorted grid voltage condition, the traditional current-control architecture is unable to provide non-oscillatory currents without a positive sequence extraction mechanism. With the proposed architecture the estimator gives the positive sequence voltage, so currents are always balanced.

4. CONCLUSION

This paper presented a Lyapunov energy function-based current-control architecture embedded with an internal model-based grid voltage estimator. The proposed estimation technique can be utilized as an alternative for conventional PLL structures that require a

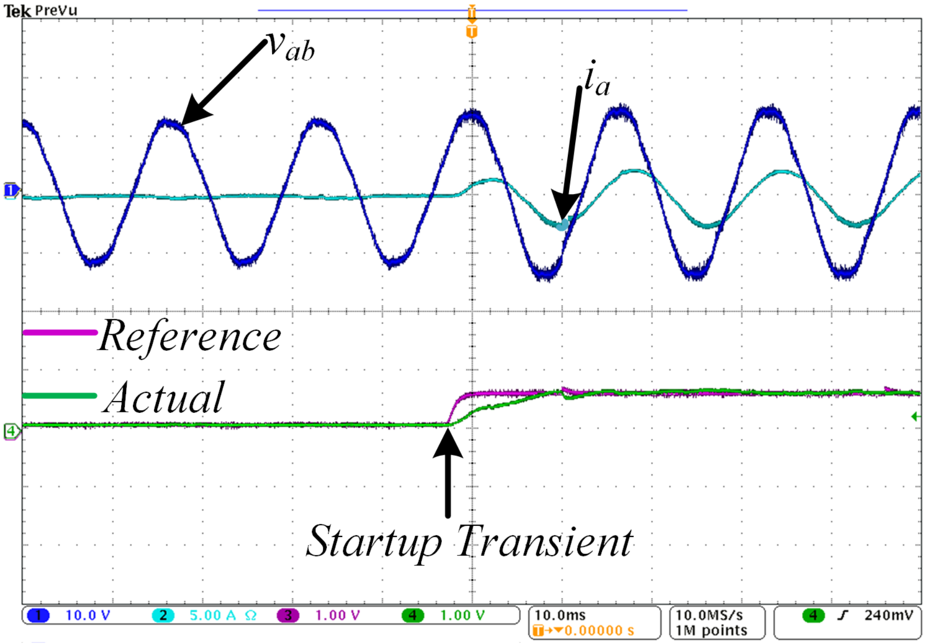

Figure 18. Transient performance of a traditional current control architecture in from experiment (i_a: 5A/div)

dedicated voltage sensing unit. The reported current-control come estimation technique is specifically useful in cases where the grid voltage sensor fails during the operation of the inverter. During those times with the proposed scheme, a seamless power transfer with all the reported performance criteria is possible. It has been shown that the current control along with the estimation is able to extract the positive sequence grid voltage along with the unit vectors required for the phase locking. The overall system modeling, compensator designs for the estimator, and the selection criteria for the Lyapunov current controller gain has been presented. The modeling gave the bounds for the selection of the Lyapunov current-controller gain. The sensitivity analysis shows the effect of parameter mismatch (i.e. the error in the estimated grid voltage due to variation of equivalent inductance and resistance). Detailed simulation results along with experimental verifications for various case studies were presented. The results show consistency with the theory and support the simulation and the experimental results, thereby showing the efficacy of the proposed Lyapunov-based current-control architecture embedded with the grid voltage estimator.

BIBLIOGRAPHY

[1] P. Zhang, Y. Wang, W. Xiao, and W. Li, “Reliability evaluation of grid-connected photovoltaic power systems,” *IEEE Transactions on Sustainable Energy*, vol. 3, pp. 379–389, Jul 2012.

[2] S. Yang, D. Xiang, A. Bryant, P. Mawby, L. Ran, and P. Tavner, “Condition monitoring for device reliability in power electronic converters: A review,” *IEEE Transactions on Power Electronics*, vol. 25, pp. 2734–2752, Nov 2010.

[3] F. Chan and H. Calleja, “Reliability estimation of three single-phase topologies in grid-connected PV systems,” *IEEE Transactions on Industrial Electronics*, vol. 58, pp. 2683–2689, Jul 2011.

[4] E. Twining and D. G. Holmes, “Grid current regulation of a three-phase voltage source inverter with an LCL input filter,” *IEEE Transactions on Power Electronics*, vol. 18, pp. 888–895, May 2003.

[5] M. Castilla, J. Miret, J. Matas, L. G. de Vicuna, and J. M. Guerrero, “Linear current control scheme with series resonant harmonic compensator for single-phase grid-connected photovoltaic inverters,” *IEEE Transactions on Industrial Electronics*, vol. 55, pp. 2724–2733, Jul 2008.

[6] M. Castilla and J. Miret and J. Matas and L. G. de Vicuna and J. M. Guerrero, “Control design guidelines for single phase grid-connected photovoltaic inverters with damped resonant harmonic compensators,” *IEEE Transactions on Industrial Electronics*, vol. 56, pp. 4492–4501, Nov 2009.

[7] J. M. Espi, J. Castello, R. Garcia-Gil, G. Garcera, and E. Figueres, “An adaptive robust predictive current control for three-phase grid-connected inverters,” *IEEE Transactions on Industrial Electronics*, vol. 58, pp. 3537–3546, August 2011.

[8] S. Golestan and J. M. Guerrero, “Conventional synchronous reference frame phase-locked loop is an adaptive complex filter,” *IEEE Transaction on Industrial Electronics*, vol. 62, pp. 1679–1682, Mar 2012.

[9] T. Thacker, D. Boroyevich, R. Burgos, and F. Wang, “Phase-locked loop noise reduction via phase detector implementation for single-phase systems,” *IEEE Transactions on Industrial Electronics*, vol. 58, pp. 2482–2490, Jun 2011.

[10] R. M. S. Filho, P. F. Seixas, P. C. Cortizo, L. A. B. Torres, and A. F. Souza, “Comparison of three single-phase PLL algorithms for UPS applications,” *IEEE Transactions on Industrial Electronics*, vol. 55, pp. 2923–2932, Aug 2008.

[11] M. Karimi-Ghartemani, “Linear and pseudo linear enhanced phased locked loop (ePLL) structures,” *IEEE Transactions on Industrial Electronics*, vol. 61, pp. 1464–1474, Mar 2014.

[12] S. Golestan, M. Monfared, F. D. Freijedo, and J. M. Guerrero, “Design and tuning of a modified power-based PLL for single-phase grid-connected power conditioning systems,” *IEEE Transactions on Power Electronics*, vol. 27, pp. 3639–3650, Aug 2012.

[13] J. R. et al., “Predictive current control of a voltage source inverter,” *IEEE Transactions on Industrial Electronics*, vol. 54, pp. 495–503, February 2007.

[14] S. Kouro, R. V. P. Cortes, U. Ammann, and J. Rodriguez, “Model predictive control: A simple and powerful method to control power converters,” *IEEE Transactions on Industrial Electronics*, vol. 56, pp. 1826–1838, June 2009.

[15] J. M. Espi, J. Castello, R. Garcia-Gil, G. Garcera, and E. Figueres, “An adaptive robust predictive current control for three phase grid-connected inverters,” *IEEE Transactions on Industrial Electronics*, vol. 58, pp. 3537–3546, Aug 2011.

[16] H. Komurcugil, “Improved passivity-based control method and its robustness analysis for single-phase uninterruptible power supply inverters,” *IET Power Electronics*, vol. 8, pp. 1558–1570, Mar 2015.

[17] H. Komurcugil, N. Altin, S. Ozdemir, and I. Sefa, “Lyapunov-function and proportional-resonant-based control strategy for single-phase grid-connected VSI with LCL filter,” *IEEE Transactions on Industrial Electronics*, vol. 63, pp. 2838–2849, May 2016.

[18] D. G. Holmes and T. A. Lipo and B. P. McGrath and W. Y. Kong, “Optimized design of stationary frame three phase AC current regulators,” *IEEE Transactions on Power Electronics*, vol. 24, pp. 2417–2426, May 2016.

[19] I. Sefa, S. Ozdemir, H. Komurcugil, and N. Altin, “An enhanced lyapunov-function based control scheme for three-phase grid-tied vsi with lcl filter,” *IEEE Transactions on Sustainable Energy*, vol. 10, pp. 504–513, April 2019.

[20] S. Chattopadhyay and V. Ramanarayanan, “Digital implementation of a line current shaping algorithm for three phase high power factor boost rectifier without input voltage sensing,” *IEEE Transactions on Power Electronics*, vol. 19, pp. 709–721, May 2004.

[21] J. Noguchi, H. Tomiki, S. Kondo, and I. Takahashi, “Direct power control of PWM converter without power-source voltage sensors,” *IEEE Transactions on Industry Applications*, vol. 34, pp. 473–479, May/Jun 1998.

[22] M. Malinowski, M. P. Kazmierkowski, S. Hansen, F. Blaabjerg, and G. D. Marques, “Virtual-flux-based direct power control of three-phase PWM rectifiers,” *IEEE Transactions on Industry Applications*, vol. 37, pp. 1019–1027, Jul./Aug 2001.

[23] P. Antoniewicz and M. Kazmierkowsk, “Virtual-flux-based predictive direct power control of ac/dc converters with online inductance estimation,” *IEEE Transactions on Industrial Electronics*, vol. 55, pp. 4381–4390, Dec 2008.

[24] L. A. Serpa, S. Ponnaluri, P. M. Barbosa, and J. W. Kolar, “A modified direct power control strategy allowing the connection of three-phase inverters to the grid through LCL-filters,” *IEEE Transactions on Industry Applications*, vol. 43, pp. 1388–1400, Sep/Oct 2007.

[25] J. A. Suul, A. Luna, P. Rodriguez, and T. Undeland, “Voltage sensor-less synchronization to unbalanced grids by frequency-adaptive virtual flux estimation,” *IEEE Transactions on Industrial Electronics*, vol. 59, pp. 2910–2923, Jul 2012.

[26] L. Harnefors and H. Nee, “Model-based current control of ac machines using the internal model control method,” *IEEE Transactions on Industry Applications*, vol. 34, pp. 133–141, Jan 1998.

[27] M. Yazdanian and A. Mehrizi-Sani, “Internal model-based current control of the rl filter-based voltage-sourced converter,” *IEEE Transactions on Energy Conversion*, vol. 29, pp. 873–881, Dec 2014.

[28] S. Leitner, M. Yazdanian, S. Ziaeinejad, A. Mehrizi-Sani, and A. Muetze, “Internal model-based active resonance damping current control of a grid-connected voltage-sourced converter with an LCL filter,” *IEEE Transactions on Power Systems*, vol. 33, pp. 6025–6036, Nov 2018.

[29] P. Mattavelli and S. Buso, *Digital Control in Power Electronics*. Morgan and Claypool Publication, 2006.

[30] H. Landau, “Sampling, data transmission, and the nyquist rate,” in *Proc.IEEE*, June 1967.

[31] P. Rodriguez, R. Teodorescu, I. Candela, A. V. Timbus, M. Liserre, and F. Blaabjerg., “New positive-sequence voltage detector for grid synchronization of power converters under faulty grid conditions,” in *Proc. 37th Annual IEEE Power Electronics Specialist Conf.*, Jeju, South Korea, June 2006.

[32] H. K. Khalil, *Nonlinear Systems*. Englewood Cliffs, NJ: Prentice-Hall, 1995.

[33] P. Rodriguez, A. Luna, M. Ciobotaru, R. Teodorescu, and F. Blaabjerg, “Advanced grid synchronization system for power converters under unbalanced and distorted operating conditions,” in *Proc. 32nd IEEE-IECON.*, Paris, France, November 2006, pp. 5173–5178.

[34] P. Rodriguez, A. Luna, I. Candela, R. Mujal, R. Teodorescu, and F. Blaabjerg, “Multiresonant frequency-locked loop for grid synchronization of power converters under distorted grid conditions,” *IEEE Transactions on Industrial Electronics*, vol. 58, pp. 127–138, January 2011.

[35] V. R. Chowdhury, S. Mukherjee, and J. Kimball, “A voltage sensorless control of a three phase grid connected inverter based on Lyapunov energy function under unbalanced grid voltage condition,” in *Proc. 10th IEEE Energy Conversion Congress and Exposition*, Portland, USA, September 2018.

III. OPTIMAL BATTERY SCHEDULING IN A MICROGRID BASED ON MARKOV DECISION PROCESS FOR COST MINIMIZATION

ABSTRACT

With a focus of reducing emission due to power production from fossil fuels, emphasis on renewable energy based resources are gaining more importance in recent years. Photovoltaic power generation scheme becomes one of the viable option for the power production. However, the intermittent nature of the photovoltaic system makes it immensely challenging to match the power available and the load demand. Therefore, to mitigate this issue, this paper discusses the possibility of having a battery backup for such a system with a framework based on Markov Decision Process (MDP) to schedule the battery. Degradation of the battery is modelled mathematically and added as a penalty to the optimization so as to get the real cost of power production. The battery degradation based on the battery chemistry is first studied then an equivalent electrical modeling has been accomplished to modify the cost function. The rate structure selected in this paper is from (Rolla Municipal Utilities) and the cost function is optimized. Then a sensitivity analysis based on different components of the rate structure along with the battery cost is performed to understand it effect and generalize it. The discussed control algorithm is tested on a system comprising of a grid, a photovoltaic generation, local loads and a battery energy storage system.

1. INTRODUCTION

Focusing on the issue of reduction of carbon emission due to power production, renewable resources like solar and wind have gained immense popularity in recent times. However, energy produced from renewable resources is inherently intermittent in nature

[1–6, 11]. The peak loads at any point of time in a microgrid must be matched by the renewable energy sources so as to reduce the demand charge from the main grid. However, matching the customer load peaks exactly by the renewable instantaneously is not possible. Therefore, situations arise when the demand is higher and the supply from the renewables are lower and when the supply from the renewable resources are higher but the load demand is lower. To mitigate such a situation, requirement for a battery energy storage system becomes inevitable [12]. On a typical day, both the solar energy and consumer load profiles are stochastic in nature. Therefore a smart control architecture to successfully charge and discharge the battery is required to match the demand and supply and also at the same time reduce the cost.

A battery management system can address the problem of scheduling the battery assuming that the future load and solar data is available to the operator [1,3]. To incorporate the stochastic nature of the PV and the load, either dynamic programming or forecast based optimization like MDP has to be utilized. In this paper, the latter methodology is used and optimal scheduling of battery is accomplished. The degradation model of the battery has been accomplished as presented in [13]. The battery chemistry is taken into consideration and the degradation of the battery is modelled based on the solid electrolyte (SEI) layer formation. The degradation of the battery is determined using a single particle (SP) model coupled with a pseudo-two-dimensional ($P2D$) physics-based model. Mathematical models based on the previous concept are developed to simplify calculations. The algorithm followed in this paper has three parts: Rolling horizon Markov Decision Process, Day-ahead load forecasting and Day-ahead solar forecasting. A sensitivity analysis for the overall cost based on the rate structure's different components i.e. buying price, selling price, demand charge and the battery cost is also presented. Such an analysis for the overall cost is pursued to understand the nature of variation of the overall cost in terms of the above mentioned parameters.

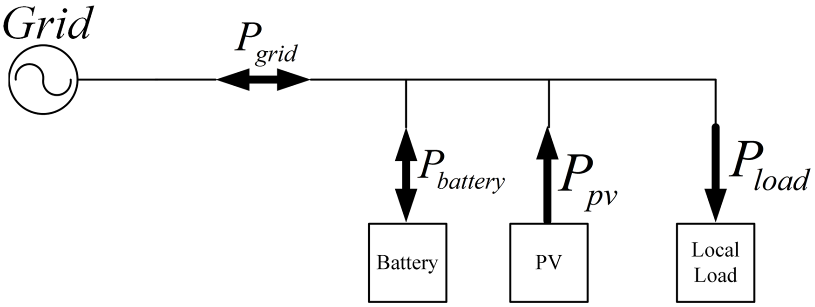

Figure 1. Simplified block diagram of the overall control architecture

The rest of the paper is arranged as follows. Section 2 presents the simplified system modelling, Section 3 presents the mathematical details of how the battery degradation modelling has been accomplished, Section 4 presents discussion on the Markov decision process and how it is utilized to modify the cost function and incorporate the battery degradation cost. Section 4 also have three subsections: subsection 4.1 presents how to model the battery as an energy source, subsection 4.2 presents how the battery actions are taken and subsection 4.3 presents the overall modified cost function. Section 5 presents the sensitivity analysis for the various components of the rate structure along with battery degradation cost. Section 6 presents the results and discussion followed by conclusion in Section 7.

2. SIMPLIFIED SYSTEM MODELLING

The system under consideration is presented with a simplified block diagram in Figure 1. The allowable power flow is indicated by the arrows in Figure 1. The convention followed is: the battery can either charge or discharge depending upon the constraints, the PV can only supply power and the grid can either supply or sink power from the system. Let us now define the powers from the various sources as; grid power (P_{grid}), battery power ($P_{battery}$), the power from the PV system (P_{PV}) and power from the load as (P_{load}). The convention followed in this paper is positive (P_{grid}) implies power drawn from the grid and positive ($P_{battery}$) implies battery is being discharged. For ideal cases, the battery can be charged or discharged to any extent possible. However, in all practical scenarios, the battery operation is limited by some constraints. In this paper, the constraints on the battery are: battery must operate within a minimum and a maximum power range and state of charge (SOC) of the battery must be maintained within a certain value. Also the overall constraint for the system under consideration is that the load must always be supplied. To summarize these constraints, we have;

$$P_{load} = P_{battery} + P_{grid} + P_{PV} \tag{1}$$

$$SOC_{\min} \leq SOC(k) \leq SOC_{\max} \tag{2}$$

$$P_{battery}^{\min} \leq P_{battery} \leq P_{battery}^{\max} \tag{3}$$

where

$SOC_{\min}$ and $SOC_{\max}$ are the minimum and the maximum limits of the allowable battery SOC

$P_{battery}^{\min}$ and $P_{battery}^{\max}$ are the minimum and the maximum allowable battery powers

k is the minimum time step.

The next section presents the philosophy and the equations followed to model the battery degradation empirically and obtain a modified cost function for the MDP optimization.

3. BATTERY DEGRADATION MODELING

The equations pertaining to the battery degradation modelling has been presented and discussed in this section. The degradation physics considered here are due to formation of solid electrolyte interface (SEI) layer. A schematic diagram of SEI formation, growth, and additional formation and its growth due to crack propagation has been reported in [13]. Qualitatively, during the formation cycle, a uniform SEI layer containing Li_2O, LiF, and Li_2CO_3 is formed on freshly exposed particle surfaces with the initial crack surface due to electrolyte reduction. With the usage of the battery, the SEI layer tends to grow, particularly when the battery is operated under higher temperature. The induced stress due to diffusion causes cracks to propagate on the particle surface, creating new surfaces that are exposed to electrolyte and on which new SEI layers are formed. The initial SEI layer thickness L_{SEI}^0 as presented in [13] is given by

$$L_{SEI}^0 = \frac{0.1 Q_{init} M_{SEI}}{A_{init} n_{SEI} \rho_{SEI} F} \tag{4}$$

where Q_{init} is the initial capacity before SEI layer formation cycle process is conducted, A_{init} is the particle surface area before the SEI layer formation cycle, n_{SEI} is the number of lithium moles lost for every mole of SEI layer formed, ρ_{SEI} is the SEI layer density and M_{SEI} is the molecular weight of compounds constituting the SEI layer. In (4), is the surface area of a sphere with initial defects as presented in [8] and is quantified as presented in (5). A 10% capacity loss is assumed during the formation cycle as presented in [13]. Now as the battery starts cycling i.e. charging/discharging operations, the SEI layer starts to grow along with the initial defects and form cracks due repeated stress on active material particles. Also the initial surface area of the single particle is the

$$A_{init} = 4\pi r_n^2 (1 + 2\rho_{cr} l_{cro} a_o) \tag{5}$$

where r_n is the particle radius, ρ_{cr} is the number of cracks per unit area of particle, l_{cro} is the initial crack width and a_o is the initial crack length. The values for the various parameters mentioned above is presented in Table 1.

Table 1. Battery Parameters

Parameter	**Value**
Q_{init}	339×10^{-3} Ahg^{-1}
M_{SEI}	78.89 g/mol
n_{SEI}	2
ρ_{SEI}	$2.11{\times}10^{6}gm^{-}3$
F	96.487×10^{3} C/mol
r_n	5×10^{-6} m
ρ_{cr}	$2.542{\times}10^{18}m^{-}2$
l_{cro}	$2{\times}10^{-9}m$
a_o	$2{\times}10^{-9}m$

Considering the above mentioned phenomenon, the battery degradation is modelled based on the chemistry of the battery and simulated via MATLAB®/Simulink®. The modelled battery is loaded over the full range of operation and the data is obtained. From the preliminary discussions it is observed that the degradation of the battery due its usage for charging/discharging is a function of initial capacity (Q_{init}), power exchanged from the battery ($P_{battery}$) and the state of charge (SoC) of the battery. More details on how exactly the crack propagates and ultimately the battery life is lost is beyond the scope of this paper and is detailed out in [13]. As mentioned earlier, to electrically model the degradation phenomenon, the data of the battery, the chemical equations of the battery are solved numerically through MATLAB® programming. The battery parameters chosen for the simulation can be found in Table I of [13]. Using the battery data and the curves presented in the literature, an empirical curve fitting toolbox was utilized in MATLAB®/Simulink® to approximate the battery behavior by polynomial equations. From the data it is observed that the degradation of the battery is a function of the state of the health (SoH) of the battery. This is equivalent to saying that the degradation of the battery is a function of the starting capacity of the battery or the initial capacity (Q_{init}). Also it is observed that degradation of a battery is a function of power exchanged from the battery ($P_{battery}$) and the state of charge (SoC) of the battery. From the battery characteristics, the degradation of the battery is plotted as a function of $P_{battery}$ and SOC with Q_{init} as the parameter. Now from the data, a family of surfaces are plotted whose equation is given by;

$$\begin{aligned}\Delta Q &= a_o(Q_{init}) + a_1(Q_{init})P_{battery} + a_2(Q_{init})SoC \\ &+a_3(Q_{init})P_{battery}^2 + a_4(Q_{init})(P_{battery}{\times}SoC) \\ &+a_5(Q_{init})P_{battery}^3 + a_6(Q_{init})(P_{battery}^2{\times}SoC) \\ &+a_7(Q_{init})P_{battery}^4 + a_8(Q_{init})(P_{battery}^3{\times}SoC)\end{aligned} \tag{6}$$

The expression for the degradation in (6) is a non-linear function where the coefficients a_o, a_1,... a_8 are functions of the initial capacity Q_{init} of the battery. As the coefficients are the function of the initial capacity, therefore a family of planes are plotted and each time the operating point of the battery is changed, the equation of the plane is modified. The coefficients as mentioned before are a function of initial capacity Q_{init} and are presented. The equations and the curve fits of the first two coefficients are presented as shown in Figures 2 and 3. Other coefficients along with their curves for variations are similar in nature.

$$a_o = -0.0049Q_{init} - 0.0075 \tag{7}$$

$$a_1 = 0.0017Q_{init} + 0.0008 \tag{8}$$

$$a_2 = 0.00031Q_{init} - 0.0059 \tag{9}$$

$$a_3 = 0.021Q_{init} + 0.00029 \tag{10}$$

$$a_4 = 0.002Q_{init} - 0.00016 \tag{11}$$

$$a_5 = 0.00067Q_{init} + 0.00013 \tag{12}$$

$$\begin{aligned}a_6 &= -(4.5 \times 10^{-8})Q_{init}^2 \\ &+(1.1 \times 10^{-7})Q_{init} + 2.9 \times 10^{-8}\end{aligned} \tag{13}$$

$$a_7 = -(5.2 \times 10^{-9})Q_{init} + 1.5 \times 10^{-9} \tag{14}$$

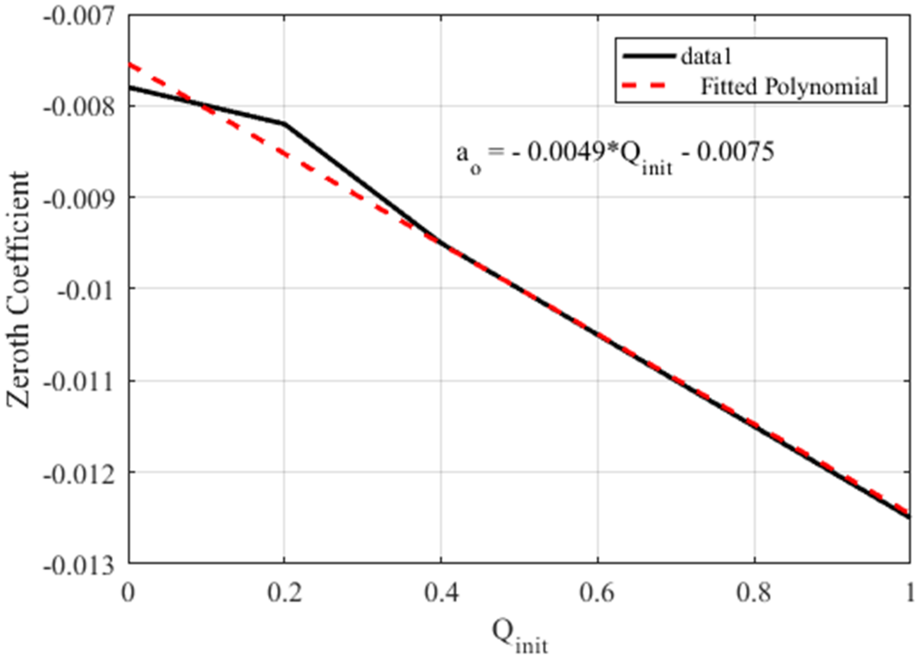

Figure 2. Curve fitting of the zeroth coefficient

$$a_8 = (2.2 \times 10^{-9})Q_{init} + 1.88 \times 10^{-9} \tag{15}$$

From the empirical curve fitting over the battery data obtained, it is observed that from (7) through (15) the coefficients of the degradation expression of (6) are dependent on the initial capacity which indicates that during a full cycle charge and discharge of the battery, there is a change in the initial capacity of the battery. This actually models the battery degradation during the battery's operation. Now any usage of battery followed by its degradation must be incurred with some cost of the battery usage. Considering the cost of a lithium ion battery of \$200/kWh with a lifetime of 10 years, the optimization is accomplished. The next section presents the details of the Markov Decision Process (MDP) which is utilized to optimize the overall cost.

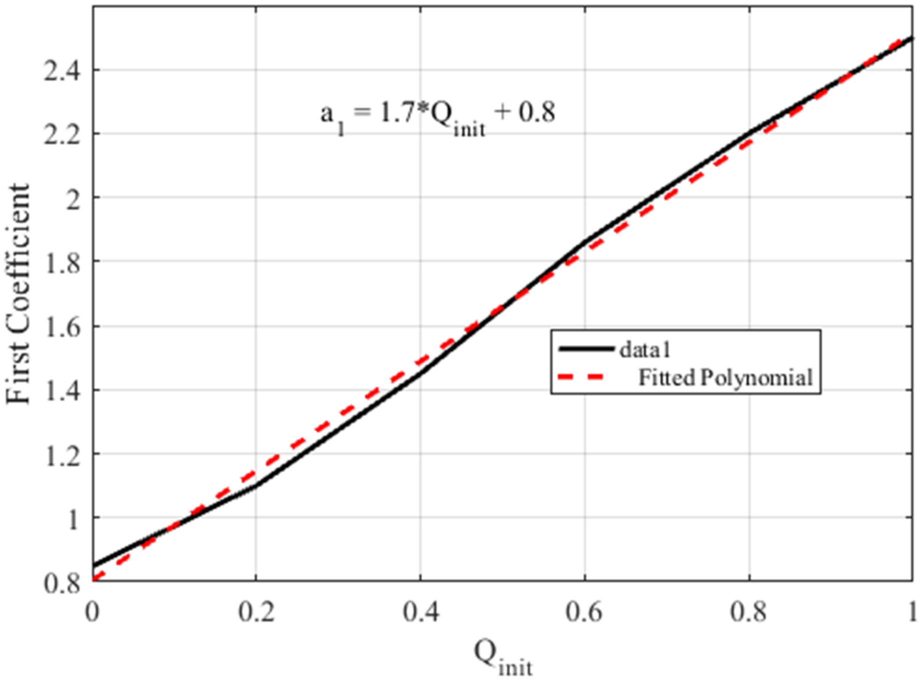

Figure 3. Curve fitting of the first coefficient

4. BATTERY ACTIONS

4.1. BATTERY AS AN ENERGY STORAGE DEVICE

The battery is considered as an energy storage device i.e. having a fixed amount of energy throughout this paper. The total energy of the battery is discretized into bins. To quantify, in terms of equation we have:

$$E_{bin} = \frac{E_{MAX} - E_{MIN}}{M} \tag{16}$$

So, a battery can have energy E_i as

$$\begin{aligned} L_i &= E_{MIN} + (i-1)E_{BIN} \\ U_i &= E_{MIN} + iE_{BIN} \\ e(t) &= \tfrac{1}{2}(U_i + L_i) \end{aligned} \tag{17}$$

where U_i is the upper limit of Energy and L_i is the lower limit of Battery Energy. Therefore, the battery can have M discrete states during the scheduling and expected energy $e(t)$ of battery would be greater than L_i and smaller than U_i. In the simulations, M is taken as 200 and E_{MAX} as 200 kWh and E_{MIN} as zero but during practical implementation, boundaries can be set on maximum and minimum energies to ensure that the battery is charged/discharged till certain levels. The next subsection elaborates the battery actions and how it is formulated to optimize the overall cost via MDP.

4.2. BATTERY ACTIONS

In the present MDP formulation scenario, the battery scheduling actions are either charging or discharging. As the battery energy is discretized into energy levels, for each state E_i, some finite discrete actions are possible. These possible actions i.e. the charge/discharge rates are chosen in a way such that there is an increment/decrement in energy E with a probability of 1. To quantify, it can be expressed as:

$$\begin{aligned} P_E &= \frac{aE_{BIN}\eta_d}{\Delta t}; a > 0 \\ P_E &= \frac{aE_{BIN}}{\eta_c \Delta t}; a < 0 \end{aligned} \tag{18}$$

Where: a = Charge/Discharge action Δt = Epoch time (15 min) η_c = Charging efficiency η_d = Discharging efficiency As was mentioned before let us define the probability of transitioning from from state E_i to E_j as

$$\begin{aligned} \delta_{ij} &= 1 \quad (i - j) = n \\ \delta_{ij} &= 0 \quad (i - j) \neq n \end{aligned} \tag{19}$$

It is observed from (19) that only discrete states are possible while transitioning from one epoch to the other as other states might not be even feasible. This type of discretization makes the problem simpler and very less computationally burdened. The next subsection presents the definition of the cost function incorporating the battery degradation cost into the MDP optimization problem.

4.3. COST FUNCTION

In this subsection, the cost function development is explained. For the current system, the total cost accumulated at each state of a certain epoch is a function of the destination state of the next epoch and the current action taken. However, the cost mentioned here is not the actual cost of energy production for a day. The overall cost is divided into two parts: The grid cost and the Battery cost.

The grid cost can be defined as the expected cost of transitioning from state E_i to E_j at epoch k. The power of the grid is then estimated by the constraint (1). The grid power P_G is Gaussian in nature because P_{PV} and P_L are Gaussian and P_E is fixed and can be calculated by the action taken at that epoch. Considering the above constraints, the cost function of the grid i.e. C_G is given by:

$$C_G = \begin{cases} P_G \theta_s \Delta t & P_G < 0 \\ P_G \theta_b \Delta t & 0 < P_G < \gamma \\ (P_G - \gamma)\theta_d \Delta t & P_G > \gamma \end{cases} \tag{20}$$

Where,

θ_s=Selling price per kWh

θ_b=Buying price per kWh

θ_d=Demand price per kW

γ=Threshold value for demand in kW

The values of the parameters for the rate structure are presented in Table 2. The quantity γ is the threshold value for the demand. This quantity basically indicates the average or the threshold of the peak demand over a 15 minute period throughout a month. It is calculated by taking the mean of all the peak demands in a 15 min interval of time over a one month period of time. Any power level going above this threshold limit creates a penalty for the monthly bill. In ideal case, the battery energy is utilized without having any degradation or wear and tear of the battery thereby involving no depreciation cost. However, in practical situation, the battery can only be operated with certain constraints and there is a finite degradation of the battery. To incorporate the effect of degradation within the cost function, of optimization, the battery degradation cost can be represented as:

$$C_{B/day} = \frac{\Delta Q}{\Delta Q_{\max}} C_{B/capital} \tag{21}$$

where

ΔQ_{max} = the maximum allowable degradation of the battery taken as a fraction of the battery's initial capacity (= $0.2Q_{init}$)

i = Initial energy state at epoch k

j = Final energy state at epoch $(k + 1)$

ΔQ = the degradation given by (6)

$C_{B/capital}$ = the initial capital dollar cost of the installation of the battery.

$C_{B/day}$ = the dollar cost of the battery usage for a particular day.

From the above equation, the cost is positive when $j < i$ and negative when $j > i$. The primary objective of the system is to attain least cost. Therefore, this cost term tries to attain higher SoC (State of Charge) of the battery and is estimated by considering the battery installation cost and lifetime. The total cost for transitioning from state i to j at epoch k is described as;

$$C_{ij,k} = C_G + C_{B/day} \tag{22}$$

The battery cost added with the cost obtained from the optimization gives the total cost. A rolling horizon implementation is incorporated due to the fact that the PV generation and the load power are not exactly known. Therefore, at every epoch of time step, the battery actions are modified and rescheduled.

Table 2. Demand Rate Structure Used in Simulation from (RMU)

Parameter	**Rate**
Buying Rate (θ_b)	7 ¢/kWh
Selling Rate (θ_s)	1.33 ¢/kWh
Demand Rate (θ_d)	14.5 $/kW

5. SENSITIVITY ANALYSIS

In this section, the sensitivity of the overall cost due to the variation of the parameters of the rate structure and the battery cost are presented. The rate structure utilized in this paper is from Rolla Municipal utilities (RMU) and is presented in Table 2. Each of the quantities in Table 2 are fixed and obtained from the RMU. Different utilities have different rate structures. Therefore, changing each of the parameters one by one, the cost per day of the power including battery degradation cost is presented. First, the buying price is changed between ±20% of its nominal value for the present rate structure. The variation of the buying price as a function of the cost of power in a day including the battery degradation cost is presented in Figure 4 Next the the changes in the cost of power for a day is investigated and presented for the change in the selling rate of power as presented in Figure 5 Next the demand charge of RMU is changed and the overall cost for power production is presented for a day. The corresponding result is presented in Figure 6. Though the demand charge presented in Figure 6 is that of a month, however during the simulation for a day, the demand charge is scaled down for a day. To incorporate the battery degradation cost, the energy produced from the battery is taken to be $200/kWh with a lifetime of 10 years. With this cost the optimization is accomplished as mentioned earlier. In this section, the battery cost is varied and the cost of power production is presented in Figure 7 From Figure 7, it can be concluded more the battery cost is increased, the optimization algorithm tries to use less of the battery. In this way when the battery cost exceeds a certain limit, the optimization never uses the battery and the whole power is extracted from the grid. That is why the cost of

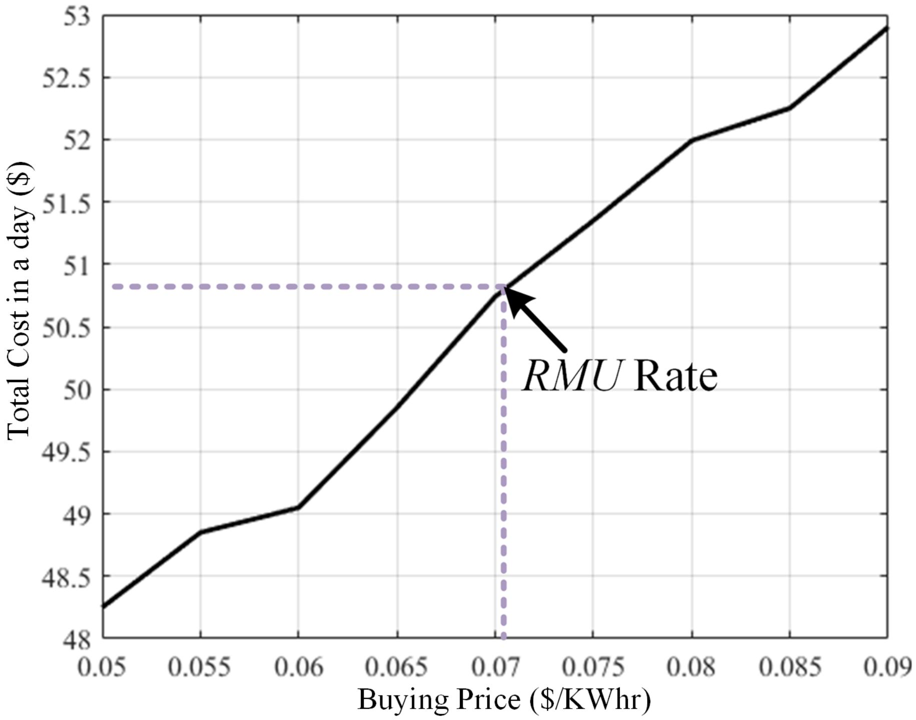

Figure 4. Change in the cost of power in a day with battery degradation with the change in the buying price

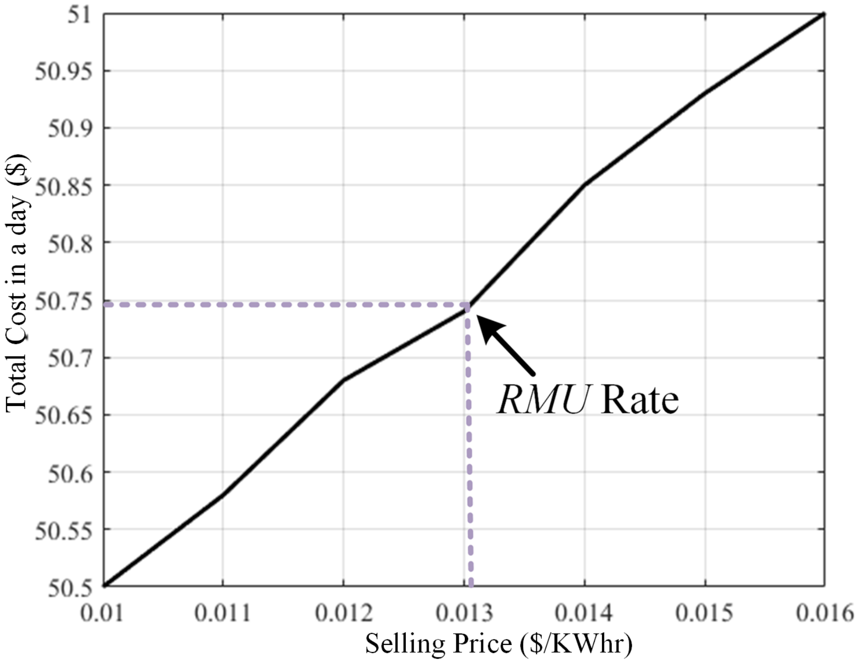

Figure 5. Change in the cost of power in a day with battery degradation with the change in the selling price

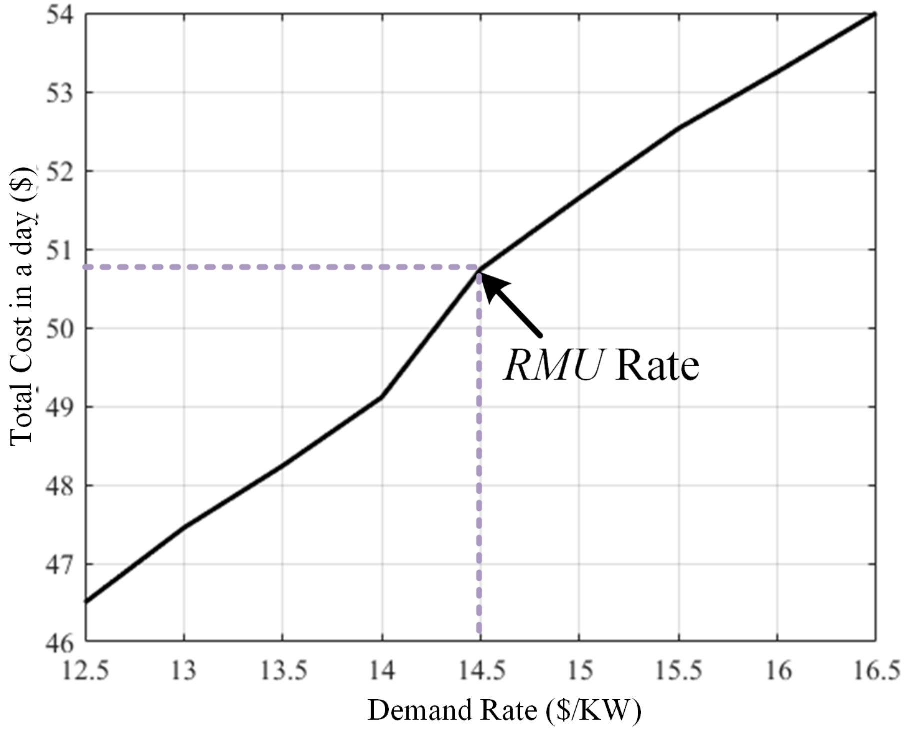

Figure 6. Cost of power production in a day with change in the demand rate

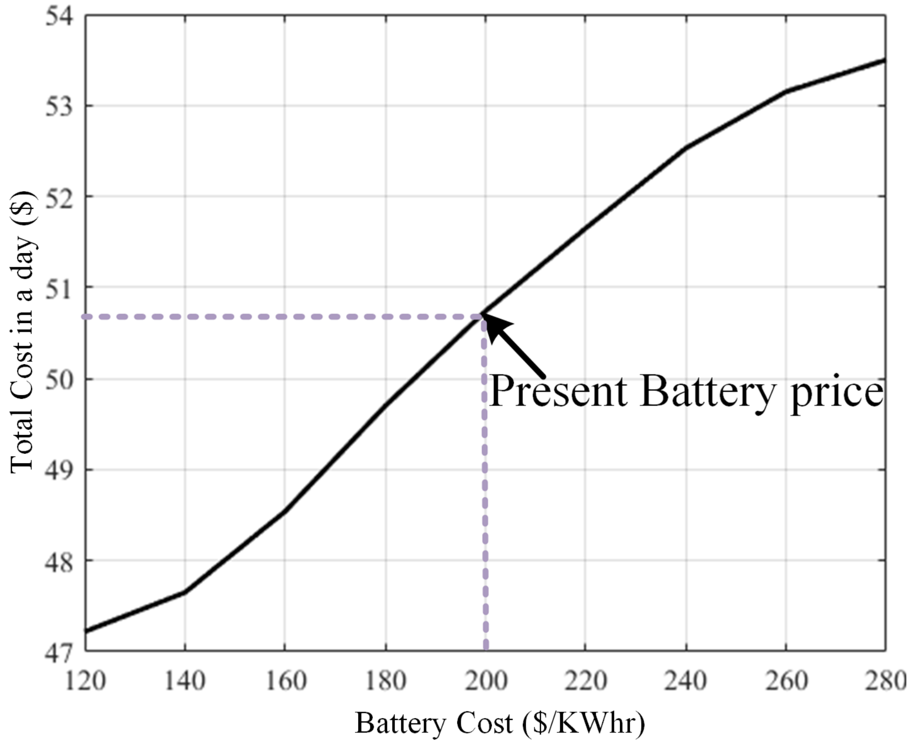

Figure 7. Change in the cost of power in a day with change in the battery cost

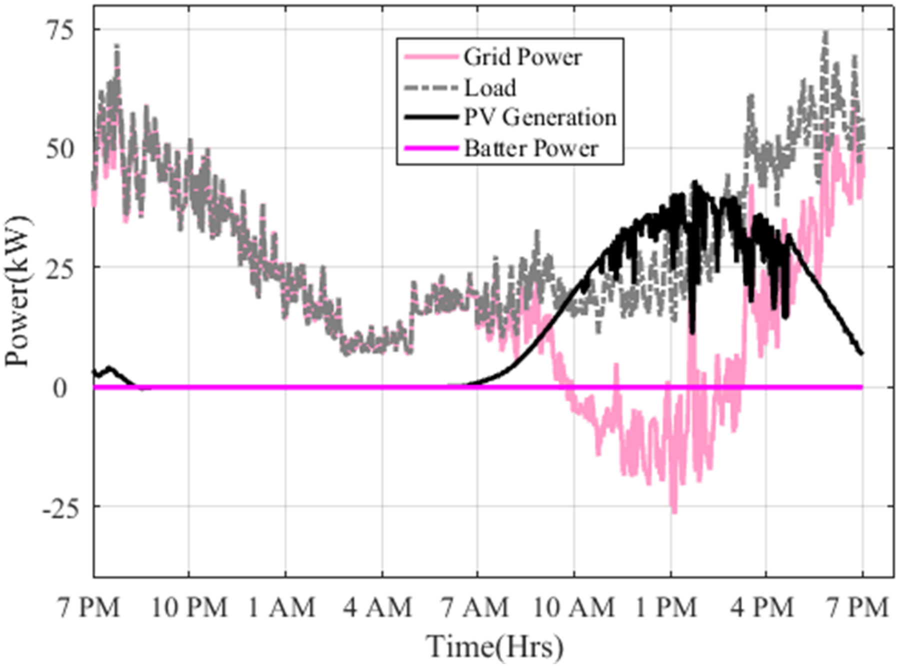

Figure 8. Power flow without consideration any battery in the system

power in a day is flattened as the battery cost is increased. For the current application, the upper threshold of the battery cost is found to be $480/kWh. From the above discussions and the results presented, the trend of the cost function towards the change of the parameters of the rate structure as well as the battery cost is presented. The next section presents the results for the total cost along with the distribution of power from *PV*, grid and battery.

6. RESULTS AND DISCUSSION

Markov decision process presented in the prior section, with battery degradation incorporated is simulated and the total cost has been computed. Results showing power from different sources in the system under consideration are presented. Case study result when there is no battery is presented in Figure 8. Power from various sources for a day of simulation with the proposed method is presented. The result in Figure 8 shows the power from *PV* and grid along with the total load. Next the result for power obtained from various

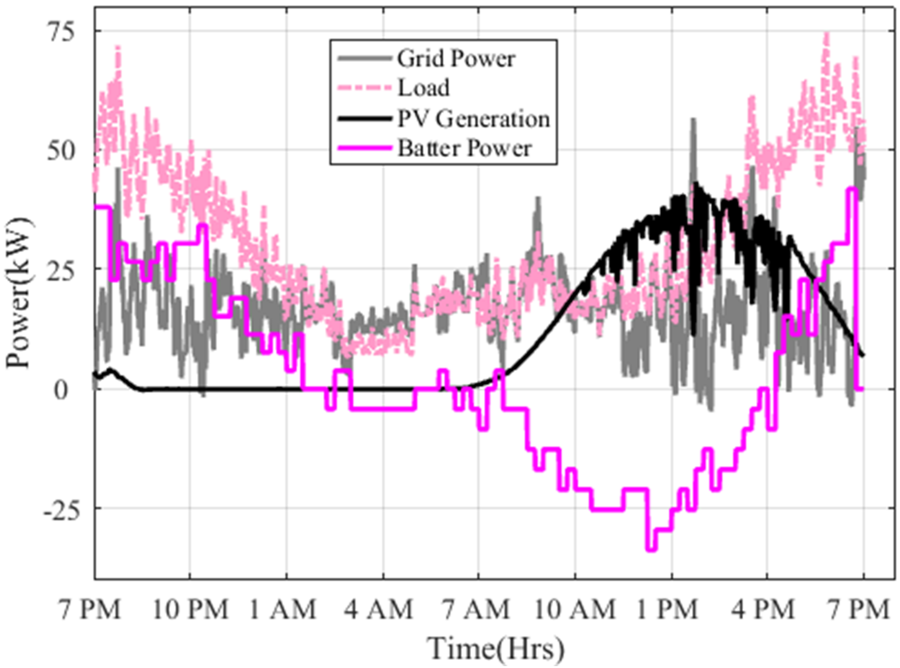

Figure 9. Power flow after scheduling with rolling horizon MDP without battery degradation

sources is presented considering the battery to be ideal i.e. no degradation in Figure 9. The presented result show that with the optimization algorithm it is possible to reduce the peaks of the load from the grid. However in Figure 9, the battery is considered to be an ideal energy source without any degradation. So in the next result presented in Figure 10, the battery is considered to be a practical source and the degradation is incorporated in the model as described in section III. The system is simulated for a day and the power obtained from various sources is presented. The above results are obtained with the rate structure utilized from Rolla Municipal Utility (RMU) whose parameters are given in Table 2. The overall dollar cost for a day without using MDP and with MDP are calculated and are presented in Table 3. In demand rate structure, the customer is penalized based on the maximum load drawn from the grid during a 15 minutes time period in a month. The

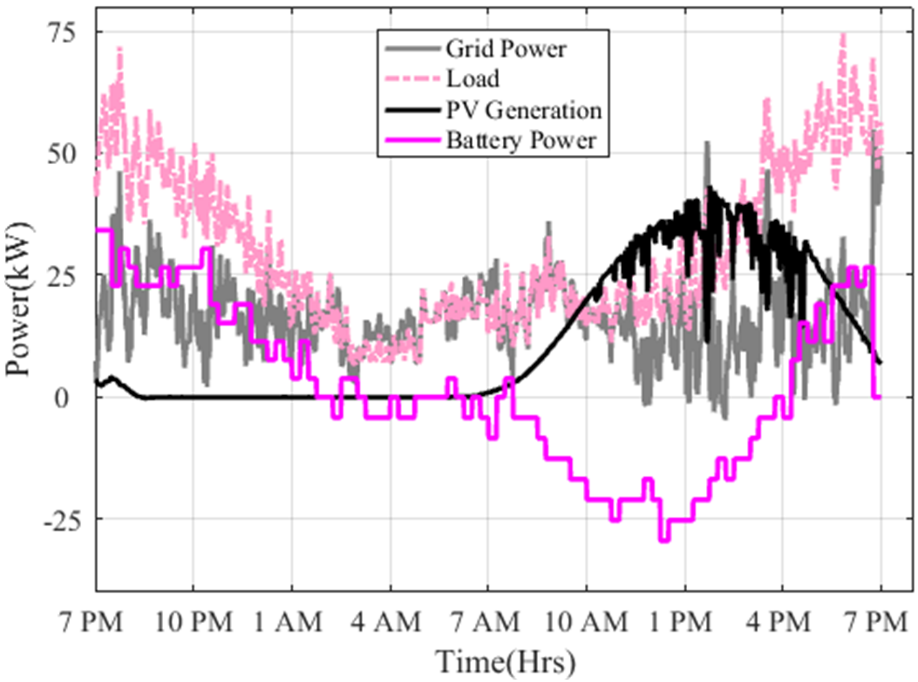

Figure 10. Power flow after scheduling with rolling horizon MDP with battery degradation

demand rate structure is typically above 12 dollars due to which it becomes the major part of the electricity bill. Therefore, peak shaving plays in an important role in reducing the billing cost as detailed in [15].

The next step is to incorporate the cost due to battery degradation and also the battery capital cost as presented in (21). The overall cost is then augmented with the term that caters for the battery degradation and convert it as a dollar cost based on the function presented in (6). It is observed from (6) that the degradation is a function of initial capacity (Q_{init}), state of charge (SoC) and the battery power ($P_{battery}$). The overall cost is modified by adding the battery degradation cost as presented in (22). The system under consideration is simulated for a day with 15 minute time interval at each epoch and the corresponding results of simulation with battery degradation incorporated has been presented in Table 3. The result showing the various powers from the grid, the power produced from the PV and

Table 3. Results

Parameter	**Value**
Load	745.7 kWh
PV Generation	256.4 kWh
Grid energy without battery bank	489.3 kWh
Grid energy with battery bank	484.9 kWh
Initial Battery energy	148 kWh
Battery energy at the end of the day	143.6 kWh
Old cost	\$61.89
Cost without battery degradation	\$47.90
Cost with battery degradation	\$50.74
Cost with changed battery power profile	\$51.85

the battery with the degradation incorporated as shown in Figure 10. From these results it is observed that the usage of battery reduces the peaks from the grid and thereby reducing the cost as presented in Table 3.

It is observed from Table 3 that the battery has depleted by 4.4 kWh. This is attributed to the fact that the battery has been depleted by 4.4 kWh i.e. to say the SOC of the battery has changed from the start of its use for that day and will be replenished by charging in a future day. Considering the degradation cost of the battery, it is observed that the usage of the battery still saves \$11.15 in a particular day than the case when no battery is present in the system. The major part of the savings by usage of the battery can be attributed to the demand charge presented in Table 2 imposed by the utilities to the customers.

Next to verify the optimization, the battery power profile obtained for the particular day is randomly changed and the new battery profile is obtained. The cost for the changed profile is presented in Table 3 and the changed battery profile is presented in Figure 11 Using these perturbed power profile for the battery, the cost of power for a day is recalculated and presented in Table 3. It is observed that the cost with the changed or non-optimized battery power profile is higher than what is obtained from the optimization. This indicates that the MDP actually gives the least and most optimized cost possible for a particular load profile

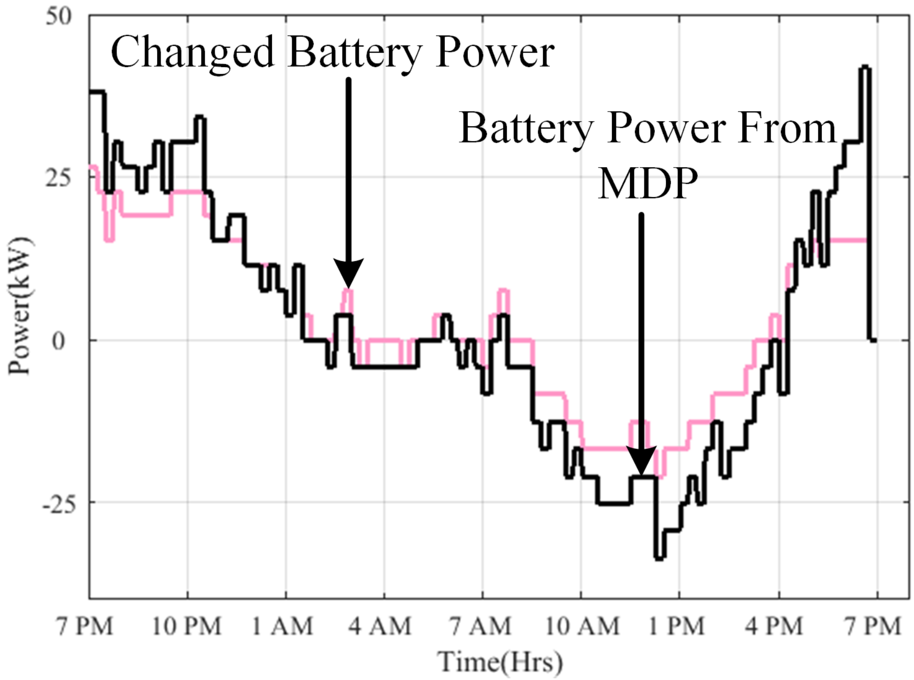

Figure 11. Power flow after scheduling with rolling horizon MDP with battery degradation for a day. From the above results presented, the overall optimization algorithm is verified and a way to utilize a battery in a micro-grid to achieve minimum cost of power at the end of the billing cycle is presented.

7. CONCLUSIONS

Battery degradation along with MDP formulation for a micro-grid system has been discussed and presented in this paper. MDP proves to be effective in peak load shaving and reduction in the overall cost. The presented work has modelled the battery degradation and shown that the overall cost has been reduced than when MDP is not being used. However, the reduction is cost is lesser than the ideal case when there is no battery degradation. The presented work is simulated for a day and the cost for the power production for a particular day has been presented from various resources and the results are presented for the cases while considering no degradation and with battery degradation. The overall methodology has been shown and proven to be effective in peak load shaving and thereby reducing the overall cost of power production. also result showing a perturbed power profile from the battery is presented and the cost is calculated for a day. The cost with the non-optimized power is observed to be higher than that obtained from the MDP optimization.

BIBLIOGRAPHY

[1] R. B. Diddigi, D. S. K. Reddy, and S. Bhatnagar, "Multi-agent qlearning for minimizing demand-supply power deficit in microgrids,", 2017.

[2] L. Raju, S. Sankar, and R. S. Milton, "Distributed optimization of solar micro-grid using multi agent reinforcement learning," *Procedia Computer Science*, vol. 46, pp. 231–239, 2015.

[3] T. Kerdphol, K. Fuji, Y. Mitani, M. Watanabe, and Y. Qudaih, "Optimization of a battery energy storage system using particle swarm optimization for stand-alone microgrids," *International Journal of Electrical Power and Energy Systems*, vol. 81, pp. 32–39, 2016.

[4] Y. Riffonneau, S. Bacha, F. Barruel, and S. Ploix, "Optimal power flow management for grid connected pv systems with batteries," *IEEE Transaction on Sustainable Energy*, vol. 2, pp. 309–320, Feb 2011.

[5] N. Amjady, "Short-term hourly load forecasting using time-series modeling with peak load estimation capability," *IEEE Transaction on Power Systems*, vol. 16, pp. 798–805, Mar 2001.

[6] S. Kouro, R. V. P. Cortes, U. Ammann, and J. Rodriguez, Modelpredictive control: A simple and powerful method to control powerconverters," *IEEE Transactions on Industrial Electronics*, vol. 56, pp.18261838, June 2009.

[7] M. P. Kazmierkowski and L. Malesani, Current control techniques forthree-phase voltage-source PWM converters: A survey," *IEEE Transactions on Industrial Electronics*, vol. 45, pp. 691703, October 1998.

[8] Deshpande, M. Verbrugge, Y.-T. Cheng, J. Wang, and P. Liu, Batterycycle life prediction with coupled chemical degradation and fatiguemechanics," *Journal of Electrochemical Society*, vol. 159, pp. 17301738, Mar 2012.

[9] S. Grillo, A. Pievatolo, and E. Tironi, Optimal storage scheduling usingMarkov decision processes," *IEEE Transaction on Sustainable Energy*, vol. 7, pp. 755764, Mar 2016.

[10] M. A. Murtaza and M. Tahir, Optimal data transmission and batterycharging policies for solar powered sensor networks using Markovdecision processes," *IEEE Wireless Communication Networking Conference*, 2013, pp. 992997.

[11] N. Amjady, "V. Blasko and V. Kaura, A new mathematical model and control ofa three phase ac-dc voltage source converter," *IEEE Transactions on Power Electronics*, vol. 12, pp. 116123, January 1997.

[12] R. Palma-Behnke, C. Benavides, F. Lanas, B. Severino, L. Reyes, J. Llanos, and D. Saez, "A microgrid energy management system based on the rolling horizon strategy," *IEEE Transactions on Smart Grid*, vol. 4, pp. 996–1006, 2013.

[13] J. Li, K. Adewuyi, N. Lotfi, R. Landers, and J. Park, "A single particle model with chemical/mechanical degradation physics for lithium ion battery state of health (soh) estimation," *Applied Energy*, vol. 212, pp. 1178–1190, Feb 2018.

[14] M. Puterman, *Markov Decision Process*. John Wiley and Sons, Inc. New York, NY, USA, 1994.

[15] P. Jain, J. A. Mueller, J. Park, and R. Landers, Battery optimizationin microgrids using Markov decision process integrated with load andsolar forecasting," *9th IEEE International Symposium on Power Electronics for Distributed Generation Systems (PEDG)*, June 2018.

SECTION

2. CONCLUSION

This dissertation proposed three new methodologies to operate a grid connected system more efficiently.

A new estimation technique for the extraction of equivalent resistance and reactance for a three-phase grid connected inverter with RL filter has been proposed. With the proposed estimation technique, it is possible to online monitor the equivalent impedance and adaptively change the plant parameters. The performance is verified via computer simulations, and various case study results are presented. The proposed estimation technique has also been verified on a reduced-scale laboratory prototype, and the performance is verified. The estimation technique presented shows stable performance when applied to a parameter-dependent control architecture.

In the second work presented, a Lyapunov energy function-based current-control architecture embedded with an internal model-based grid voltage estimator is proposed. The proposed estimation technique can be utilized as an alternative for conventional PLL structures that require a dedicated voltage sensing unit. The reported current-control come estimation technique is specifically useful in cases where the grid voltage sensor fails during the operation of the inverter. During those times with the proposed scheme, a seamless power transfer with all the reported performance criteria is possible. It has been shown that the current control along with the estimation is able to extract the positive sequence grid voltage along with the unit vectors required for the phase locking. The overall system modeling, compensator designs for the estimator, and the selection criteria for the Lyapunov current controller gain has been presented. The modeling gave the bounds for the selection of the Lyapunov current-controller gain. The sensitivity analysis shows the effect of parameter mismatch (i.e. the error in the estimated grid voltage due to variation of equivalent inductance and resistance). Detailed simulation results along with experimental verifications for various case studies were presented. The results show consistency with the theory and support the simulation and the experimental results, thereby showing the efficacy of the proposed Lyapunov-based current-control architecture embedded with the grid voltage estimator.

Finally, in the last work, battery degradation along with MDP formulation for a micro-grid system has been discussed and presented. MDP proves to be effective in peak load shaving and reduction in the overall cost. The presented work has modelled the battery degradation and shown that the overall cost has been reduced than when MDP is not being used. However, the reduction is cost is lesser than the ideal case when there is no battery degradation. The presented work is simulated for a day and the cost for the power production for a particular day has been presented from various resources and the results are presented for the cases while considering no degradation and with battery degradation. The overall methodology has been shown and proven to be effective in peak load shaving and thereby reducing the overall cost of power production. also result showing a perturbed power profile from the battery is presented and the cost is calculated for a day. The cost with the non-optimized power is observed to be higher than that obtained from the MDP optimization.

BIBLIOGRAPHY

[1] M. H. Nehrir, C. Wang, K. Strunz, H. Aki, R. Ramakumar, J. Bing, Z. Miao, and Z. Salameh, A review of hybrid renewable/alternative energy systems for electric power generation: Configurations, control and applications," *IEEE Transactions on Sustainable Energy*, vol. 2, no. 4, pp. 392403, Oct. 2011.

[2] M.P. Kazmierkowski, L. Malesani, Current control techniques for three-phase voltage-source PWM converters: a survey" *IEEE Transactions on Industrial Electronics*, vol. 45, no. 5, pp. 691703, Oct 1998.

[3] F. Blaabjerg, R. Teodorescu, M. Liserre, and A. V. Timbus, Overview of control and grid synchronization for distributed power generation systems, *IEEE Transactions on Industrial Electronics*, vol. 53, no. 5, pp. 1398-1409, Oct. 2006.

[4] M. Karimi-Ghartemani and M. R. Iravani, A method for synchronization of power electronic converters in polluted and variable-frequency environments, *IEEE Transactions Power System*, vol. 19, no. 3, pp. 1263-1270, Aug. 2004.

[5] M. Zhixin, F. Lingling, D. Osborn, and S. Yuvarajan, Wind farms with HVDC delivery in inertial response and primary frequency control, *IEEE Transactions on Energy Conversion*, vol. 25, no. 4, pp. 1171-1178, Dec. 2010.

[6] X. Yu, A. M. Khambadkone, H. Wang, and S. T. S. Terence, Control of parallelconnected power converters for low-voltage microgridPart I: A hybrid control architecture, *IEEE Transactions on Power Electronics*, vol. 25, no. 12, pp. 2962-2970, Dec. 2010.

[7] J. M. Guerrero, L. G. de Vicuna, J. Matas, M. Castilla, and J. Miret, Decentralized Control of Parallel Operation of Distributed Generation Inverters Using Resistive Output Impedance, *IEEE Transactions on Industrial Electronics*, vol. 54, no. 2, pp. 994-1004, April. 2007.

[8] P. C. Loh, M. J. Newman, D. N. Zmood, and D. G. Holmes, A comparative analysis of multiloop voltage regulation strategies for single and three-phase UPS systems, *IEEE Transactions on Power Electronics*, vol. 18, no. 5, pp. 1176-1185, Sep. 2003.

[9] C.-L. Chen, Y. Wang, J.-S. Lai, Y.-S. Lee, and D. Martin, Design of parallel inverters for smooth mode transfer microgrid applications, *IEEE Transactions on Power Electronics*, vol. 25, no. 1, pp. 6-15, Jan. 2010.

[10] D. De and V. Ramanarayanan, A proportional multiresonant controller for threephase four-wire high-frequency link inverter, *IEEE Transactions on Power Electronics*, vol. 25, no. 4, pp. 899-906, Apr. 2010.

VITA

Vikram Roy Chowdhury received the B.Tech. degree from WBUT, Kolkata, India, in 2010 and the M.Tech. degree from the Indian Institute of Technology, Kharagpur, Kharagpur, India, in 2013, both in electrical engineering. He received the Doctor of Philosophy in Electrical Engineering in December 2019 from Missouri University of Science and Technology, Rolla, MO, USA. His research interests included application of power electronics to renewable energy and electric drives.